Cement and Concrete Research 187 (2025) 107705

Contents lists available at ScienceDirect

Cement and Concrete Research

journal homepage: www.elsevier.com/locate/cemconres

# Hourly three-minute creep testing of an LC3 paste at early ages: Advanced test evaluation and the effects of the pozzolanic reaction on shrinkage, elastic stiffness, and creep

Sophie J. Schmid [a], Luis Zelaya-Lainez [a], Olaf Lahayne [a], Martin Peyerl [b], Bernhard Pichler [a,*]

[a] Institute for Mechanics of Materials and Structures, TU Wien, Karlsplatz 13/202, 1040 Vienna, Austria
[b] ALAS Minerals GmbH, Unterthalhamstraße 2, 4694 Ohlsdorf, Austria

ARTICLE INFO

*Keywords:*
Limestone calcined clay cement
C-A-S-H
AFm phases
Space filling
Creep compliance

ABSTRACT

In this study, hourly three-minute creep testing is used to elucidate the evolution of the viscoelastic behavior of cement pastes produced with ordinary Portland cement (OPC), limestone Portland cement (LPC), and limestone calcined clay cement (LC3), from 1 to 7 days after production. An innovative test evaluation protocol, accounting for shrinkage, is used to identify values of the elastic modulus, the creep modulus, and the creep exponent, *without* making assumptions. The S-shaped shrinkage evolution of the LC3 paste is explained by Portlandite dissolution and the associated redistribution of chemical shrinkage-induced compressive stresses to the remaining solid skeleton. The evolution of the elastic stiffness of the LC3 paste is explained by space filling by C-A-S-H phases. The small creep compliance of the LC3 paste is explained by C-A-S-H which creeps less than C-S-H, and by AFm phases which precipitate in nanoscopic slit pores between C-S-H structures, gluing viscous interfaces.

## 1. Introduction

Limestone calcined clay cements (LC3) are an eco-friendly alternative to ordinary Portland cements (OPC) [1,2]. LC3 allows for clinker contents below 50% [3,4]. This saves some 30% to 40% of $CO_2$ emissions [5,6]. Kaolinitic clays were shown to have the highest potential for activation of pozzolanic reactivity [7]. A test method for quantifying the reactivity of calcined clay was developed [8]. As regards binder design, the clay calcination temperature, sulfate content, and alkali content count to the main impacting factors [9,10]. As regards fresh mixing, the increased water demand resulting from the calcined clay is frequently managed by means of superplasticizer dosages which are larger than those of OPC reference materials [11–13].

Several mechanical properties of LC3 materials were characterized at early and mature ages and compared with those of OPC reference materials. The compressive strength of LC3 mortars [1,14,15] and concretes [14,16,17] is (i) smaller than that of OPC references during the first week after production, and (ii) comparable or even larger than that of OPC references at the material age of 28 days. The elastic stiffness of an LC3 paste reached some 90% of that of the OPC reference some 3 days after material production [18]. The elastic stiffness of mature LC3 mortars [9] and concretes [17] is similar to that of the OPC reference materials. LC3 materials exhibit a delayed early-age shrinkage compared to OPC reference materials [9]. Shrinkage of well-hydrated LC3 mortars [9] and concretes [17] is slightly larger or comparable to that of the OPC references. The compressive creep behavior of LC3 pastes was characterized starting 28 days after production and found to be smaller than that of OPC pastes [9]. A multiscale Finite Element analysis suggested that the C-A-S-H gel of LC3 pastes creeps less than the C-S-H gel of OPC pastes [19]. To the best of the authors' knowledge, no early-age compressive creep testing campaign on an LC3 paste is documented in the literature. The present study closes this research gap by performing hourly three-minute creep testing on an LC3 paste from 1 to 7 days after paste production.

Hourly three-minute creep testing allows for quantitative characterization of the early-age evolution of non-aging creep properties of cementitious materials [20]. Every single test characterizes a *virtually constant* microstructure, because hydration cannot make a significant progress in a few minutes. Subsequent tests, in turn, characterize *different* microstructures, because the tests are separated by one hour, and this is enough time for hydration to make a significant progress. Repeated minute-long creep testing was applied to (i) OPC pastes [20,21], allowing for identification of the creep properties of microscopic OPC hydrates [22], (ii) polymer-modified cement pastes, allowing for

* Corresponding author.
*E-mail address:* bernhard.pichler@tuwien.ac.at (B. Pichler).

https://doi.org/10.1016/j.cemconres.2024.107705
Received 25 June 2024; Received in revised form 24 September 2024; Accepted 20 October 2024
Available online 6 November 2024

identification of the creep properties of microscopic polymer particles [23], (iii) alkali-activated slag mortars, showing that such materials creep more than OPC reference materials [24], (iv) OPC mortars and concretes, to demonstrate that water migrates during mixing into the porosity of oven dried aggregates, and at later stages back to the cement paste matrix driven by self-desiccation [25], (v) OPC and CEM II concretes, to develop correlation equations allowing for translating the 28 days value of the compressive strength into the corresponding 28 days value of the creep modulus, as well as an evolution function explaining how the creep modulus increases during the first four weeks after production to approach the 28 days value [26].

Minute-long creep tests were also applied for characterization of *mature* cementitious materials. This includes creep testing of miniaturized cantilever beams made of pure and slag blended OPC pastes, subjected to a point load at the free end of the cantilever, in order to study the flexural creep behavior of C-S-H [27] as well as creep recovery [28]. Macroscopic three-minute creep tests of mature OPC pastes showed that, with increasing temperature, the elastic stiffness of OPC hydrates decreases slightly and that their creep increases significantly, according to an Arrhenius law containing the activation energy of the viscosity of water [29].

As regards the evaluation of minute-long creep tests, identification of three viscoelastic properties, i.e. the elastic modulus, the creep modulus, and the creep exponent, is a challenging task, because creep strains already develop during the initial load application phase. Existing test evaluation protocols are relying on assumptions regarding either the elastic modulus [20,21,23,24,27] or the creep exponent [26,29]. This calls for an advanced test evaluation protocol which works without assumptions.

The aim of the present study is twofold: (i) the development of an advanced evaluation protocol for hourly-performed three-minute creep tests, and (ii) quantitative insight into the early-age shrinkage, elastic stiffness, and creep behavior of an LC3 paste. As regards aim (i), the here-presented creep test evaluation protocol extends that by Ausweger et al. [26], because shrinkage strains are explicitly taken into account, and because the elastic modulus, the creep modulus, and the creep exponent are identified without making assumptions about one of them. As regards aim (ii), cement pastes produced with ordinary Portland cement, limestone Portland cement (LPC), and limestone calcined clay cement are characterized by means of hourly three-minute creep testing from 1 to 7 days after production. Creep testing is accompanied by three other experimental methods. Quasi-isothermal calorimetry provides access to the heat of hydration and allows for demonstrating the pozzolanic reaction in the LC3 paste. Ultrasonic pulse velocimetry provides access to the elastic stiffness and allows for validation of the elastic moduli identified from hourly three-minute creep testing. Uniaxial compressive strength tests provide access to the strength evolution and allow for selecting load levels for hourly three-minute creep testing, which do not damage the specimens.

The manuscript is organized as follows: Section 2 introduces the tested materials and the methods used for sample preparation, test execution, and test evaluation. This section contains the advanced protocol for the evaluation of hourly-performed three-minute creep tests. Section 3 is focused on the test results and their description, without interpretation. Section 4 refers to aim (i) of the present study. It is devoted to the discussion of the advanced creep test evaluation protocol and the associated strain modeling approach. It addresses particularly the quantification of the contribution of shrinkage to the strains measured during the three-minute load plateau, the quantification of the relative contribution of the creep deformation developing during the loading phase to the creep deformation accumulated until the end of the three-minute load plateau, and the determination of viscoelastic quantities being invariant with respect to the reference time. Section 5 refers to aim (ii) of the present study. It is devoted to the discussion of the macroscopic material behavior observed during hourly three-minute creep testing. The specific behavior of the LC3 paste is related to microstructural effects resulting from the pozzolanic reaction: dissolution of Portlandite and precipitation of both C-A-S-H and AFm phases. In Section 6, the paper is closed with conclusions drawn from the results of the presented study.

**Table 1**
Composition of the three binders used.

| Binder | CEM I 52.5 R | Limestone | Calcined clay |
|---|---|---|---|
| OPC | 100%$_{mass}$ | 0%$_{mass}$ | 0%$_{mass}$ |
| LPC | 70%$_{mass}$ | 30%$_{mass}$ | 0%$_{mass}$ |
| LC3 | 70%$_{mass}$ | 15%$_{mass}$ | 15%$_{mass}$ |

**Table 2**
Chemical composition of the calcined clay.

| Calcined clay | |
|---|---|
| $SiO_2$ | 53–54%$_{mass}$ |
| $Al_2O_3$ | 41–44%$_{mass}$ |
| $Fe_2O_3$ | < 1.2%$_{mass}$ |
| $K_2O$ | < 1.3%$_{mass}$ |

**Table 3**
Chemical composition of the CEM I 52.5 R.

| CEM I 52.5 R | |
|---|---|
| Alite ($C_3S$) | 65.0%$_{mass}$ |
| Belite ($C_2S$) | 16.1%$_{mass}$ |
| Ferrite ($C_4AF$) | 10.0%$_{mass}$ |
| Aluminate ($C_3A$ cub.) | 2.2%$_{mass}$ |
| Aluminate ($C_3A$ orth.) | 3.0%$_{mass}$ |
| Lime | 2.4%$_{mass}$ |
| Portlandite | 0.1%$_{mass}$ |
| Periclase | 0.8%$_{mass}$ |
| Arcanite | 0.2%$_{mass}$ |
| Aphtithalite | 0.1%$_{mass}$ |
| Ca-Langbeinite | 0.1%$_{mass}$ |

**Table 4**
Results of particle size analysis of binder constituents: 10%, 50%, and 90% quantiles of particle size distributions, see also Fig. 1.

| Constituent | $d_{10}$ | $d_{50}$ | $d_{90}$ |
|---|---|---|---|
| CEM I 52.5 R | 2.9 μm | 13.1 μm | 30.7 μm |
| Limestone | 2.4 μm | 30.8 μm | 146.0 μm |
| Calcined clay | 1.4 μm | 6.1 μm | 18.2 μm |

## 2. Materials and methods

### 2.1. Materials

Three cementitious binders are used to produce cement pastes:

1. an ordinary Portland cement (OPC) of type CEM I 52.5 R,
2. a limestone Portland cement (LPC) containing 70 percent by mass (%$_{mass}$) OPC and 30%$_{mass}$ limestone,
3. a limestone calcined clay cement (LC3) containing 70%$_{mass}$ OPC, 15%$_{mass}$ limestone, and 15%$_{mass}$ calcined clay of type Metaver K [30],

see also Table 1. The calcined clay is a mostly amorphous, reactive Aluminum-Silicate obtained from the calcination of clay with a kaolinite content of 95%. The chemical compositions of the calcined clay and the CEM I 52.5 R are given in Tables 2 and 3, respectively.

Particle size distributions (PSD) are determined by means of a Mastersizer 3000 laser diffraction particle size analyzer, see Fig. 1. The 10% quantile of the PSD, $d_{10}$, its median, $d_{50}$, and its 90% quantile, $d_{90}$, are listed in Table 4. Calcined clay is the finest of the raw materials and CEM I 52.5 R is the intermediate, see Fig. 1. The finer 40 percent by volume (%$_{vol}$) limestone fraction is comparable to that of the CEM I 52.5 R, while the remaining 60%$_{vol}$ limestone fraction is coarser than that of the CEM I 52.5 R, see Fig. 1.

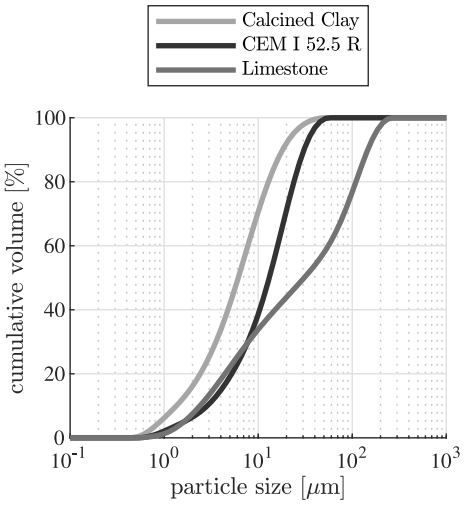


**Fig. 1.** Cumulative particle size distribution functions of binder constituents.

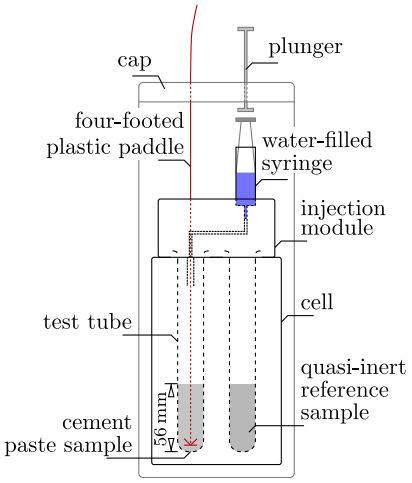


**Fig. 2.** Setup for quasi-isothermal differential calorimetry.

Cement pastes are produced from the three binders and deionized water, with an initial water-to-solid mass ratio amounting to $w/s = 0.45$. This value ensures both sufficient workability to mix a homogeneous paste and no bleeding after casting. Still, it is noted that the used calcined clay and limestone increases and decreases, respectively, the viscosity of the freshly mixed binder. During both curing and testing, the samples were conditioned at 25 °C and protected against drying.

### 2.2. Quasi-isothermal differential calorimetry

The used calorimeter of type ToniCal Trio 7339 (Toni Technik GmbH in Berlin, Germany) hosts three measuring cells for simultaneous testing of three samples. Each of the cells provides space for two test tubes: one contains the material to be tested and the other is filled with a well-hydrated, quasi-inert reference sample, see Fig. 2.

Test preparation includes inserting 10 g of a homogenized binder powder into a test tube and compacting it to a filling height of 56 mm. 4.5 g of deionized water are drawn up in a syringe. It is inserted into an injection module which is placed on top of the test tube, see Fig. 2. Thereafter, the cell is closed, followed by a waiting period of some 5 h to reach stationary conditions inside the cell, at 25 °C.

At test start, the water is injected onto the binder-powder using a plunger which runs through the cap of the cell, see Fig. 2. Mixing is performed by means of a hand-guided four-footed plastic paddle which also runs through the cap of the cell. The heat released from the exothermic binder hydration reaction results in a very subtle increase in temperature of the test specimen above 25 °C. Therefore, the test method is referred to as "quasi-isothermal".

The specific heat release rate $\dot{Q}(t)$ is recorded automatically. Every test lasts for 168 h (= seven days). $\dot{Q}(t)$ is integrated using the trapezoidal rule, in order to quantify the accumulated heat release $Q(t)$ as

$$Q(t_{i+1}) = Q(t_i) + \frac{\dot{Q}(t_{i+1}) + \dot{Q}(t_i)}{2} \times \left[t_{i+1} - t_i\right], \tag{1}$$

where $t_i$ and $t_{i+1}$ refer to two successive time instants.

Throughout this manuscript, (round) parentheses are used to show functional arguments. (Square) brackets and (curled) braces, in turn, are used to clarify the order of mathematical operations in algebraic expressions.

### 2.3. Production of cement paste cylinders for mechanical testing

The homogenized binder powder is mixed with deionized water using a lab stirrer. The obtained paste is vibrated to release entrapped air and then filled into a cylindrical plastic mold. As for protection against drying, two layers of cling film, fixed with a tape to the mold, are used to seal the specimen. Thereafter, it is stored in a climate chamber at 25 °C. Specimens are demolded some 20 h after production. The circular ends of every cylinder are manually shaved to co-planar surfaces using a utility knife [20,31,32]. The finalized specimens are either tested immediately, or they are stored under sealed conditions in the climate chamber for later testing.

### 2.4. Ultrasonics-based characterization of the elastic modulus

Ultrasonic pulse velocimetry enables non-destructive characterization of the isotropic elastic stiffness of cement paste [33]. Cylindrical specimens with a nominal height of 60 mm and a nominal diameter of 30 mm are tested. The actual height $h$, the actual diameter $d$, and the mass $m$ are measured right before testing using a digital sliding caliper and a precision scale, respectively. The tests are performed with ultrasonic square wave pulser/receiver units of type Panametrics PR5077 and an oscilloscope of type Lecroy WaveRunner 62Xi. The tests are performed once every day during the first week after material production.

The experimental setup consists of a serial arrangement of an ultrasonic pulser, a honey layer, a cling film, the specimen, another cling film, another honey layer, and an ultrasonic receiver, see Fig. 3. The honey layers ensure that ultrasonic waves are well transmitted across the interfaces between the ultrasonic heads and the specimen. The cling film prevents the honey from penetrating into the open porosity of the cement paste.

Longitudinal (index $L$) and transversal (index $T$) ultrasonic waves with a central frequency of 5 MHz are sent through the serial test setup. Corresponding *total* times of flight, $\Delta t_L$ and $\Delta t_T$, are measured. Subtracting the delay time $\Delta t_D$ which represents the time of flight through the serial test setup *without* the specimen, yields the *net* time of flight through the tested specimen. Longitudinal and transversal wave velocities, $v_L$ and $v_T$, are quantified based on the *net* time of flight:

$$v_L = \frac{h}{\Delta t_L - \Delta t_D}, \tag{2}$$

$$v_T = \frac{h}{\Delta t_T - \Delta t_D}. \tag{3}$$

The theory of elastic wave propagation through isotropic media allows for converting wave velocities into components $C_{1111}$ and $C_{1212}$ of the fourth-order elastic stiffness tensor [34–36]:

$$C_{1111} = \rho\, v_L^2, \tag{4}$$

$$C_{1212} = \rho\, v_T^2, \tag{5}$$

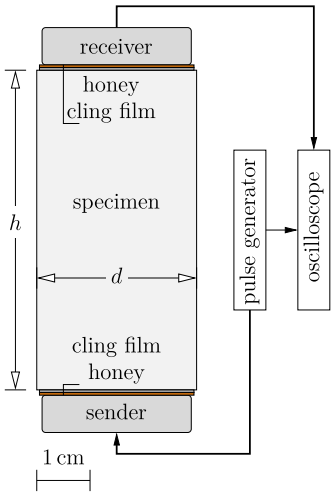


**Fig. 3.** Setup for ultrasonic pulse transmission velocimetry.

where $\rho = m/V$ denotes the mass density. The volume $V$ is equal to $h\,d^2\pi/4$. The elastic modulus $E$ is eventually quantified as [33]:

$$E = \frac{C_{1212}\left[3\,C_{1111} - 4\,C_{1212}\right]}{C_{1111} - C_{1212}}\,. \tag{6}$$

### 2.5. Uniaxial compressive strength tests

Uniaxial compressive strength tests are performed on samples which were subjected to non-destructive ultrasonic testing. The nominal height-to-diameter ratio of the cylinders amounts to 2:1. This is slender enough to ensure that friction-induced shear stresses, activated in the interfaces between the specimen and the load platens, do not have a significant influence on the results of the experiments [31]. The tests are performed on an electromechanical universal testing machine, controlled by the software testXpert of Zwick/Roell. The tests are performed 1 day, 3 days, and 7 days after material production.

The experimental setup consists of a serial arrangement of the lower load plate, a rubber pad, a metallic cylinder, two layers of Teflon, the specimen, another two layers of Teflon, another metallic cylinder, another rubber pad, and the upper load plate, see Fig. 4. The rubber pads facilitate the application of central loading by compensating for inaccuracies in the co-planarity of the loaded surfaces of the specimen. The metallic cylinders allow for imposing close-to-homogeneously distributed normal stresses on the specimens. The Teflon layers decrease friction, thus reducing the undesired, self-equilibrated shear stresses.

Prescribing a force rate of 0.5 kN/s, the maximum force sustained by the material, $\max F$, is recorded. Its compressive strength $f_c$ is equal to $\max F$ divided by the cross-sectional area of the specimen, $A = d^2\pi/4$:

$$f_c = \frac{\max F}{d^2\pi/4}\,. \tag{7}$$

### 2.6. Hourly three-minute creep testing

Three-minute creep tests are used to track the early-age development of the elastic stiffness and the creep behavior [20,26]. The tested cement paste cylinders have a nominal height of 300 mm, and a nominal diameter of 70 mm. The actual height $h$, the actual diameter $d$, and the mass $m$ are measured right before testing using a digital sliding caliper and a precision scale, respectively. Testing is carried out inside a temperature chamber. It is conditioned to 25 °C and integrated into an electromechanical universal testing machine of type Zwick/Roell

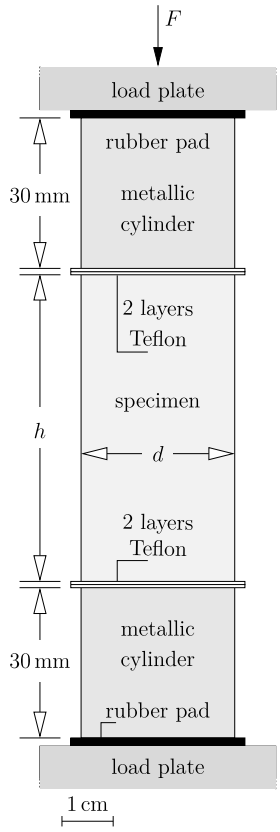


**Fig. 4.** Setup for uniaxial compressive strength tests.

50 kN. The specimen is wrapped into several layers of cling film to avoid drying. Tests are performed once every hour from 24 h after material production to a material age of 7 days. Thus, every specimen is subjected to a series of 145 creep tests.

The test setup consists of a serial arrangement of two metallic cylinders (one with and one without a bottleneck), the specimen, and another set of two metallic cylinders, see Fig. 5. The bottlenecked cylinders allow for both a near-central loading and a near-homogeneous distribution of the normal stresses imposed on the specimen. The bottlenecks make it necessary to apply a small permanent compressive normal force

$$F_{perm} = 0.2\ \text{kN} \tag{8}$$

to the specimen to keep it in an upright position. Six inductive displacement sensors of type "HBM WI/2 mm-T" measure the change of distance between two aluminum rings which are clamped by means of three screws each to the central part of the specimen. The initial distance between the aluminum rings amounts to

$$\ell_0 = 164\ \text{mm}\,. \tag{9}$$

The sensors are evenly positioned around the specimen (spacing = 60°). Their readings are amplified by means of an HBM Quantum X device and recorded using the software Catman.

For each three-minute creep test, a specific force history is prescribed (Fig. 6), which is controlled by the force cell integrated into the testing machine. The specimen is loaded with a nominal compressive force rate of 7.70 kN/s, referring to a nominal stress rate of 2 MPa/s, to the target load level. The latter increases from test to test and refers to 15% of the compressive strength of the material at the time of testing, following the example of [20]. The target load is kept constant for three minutes. Thereafter, the load is decreased to the permanent load

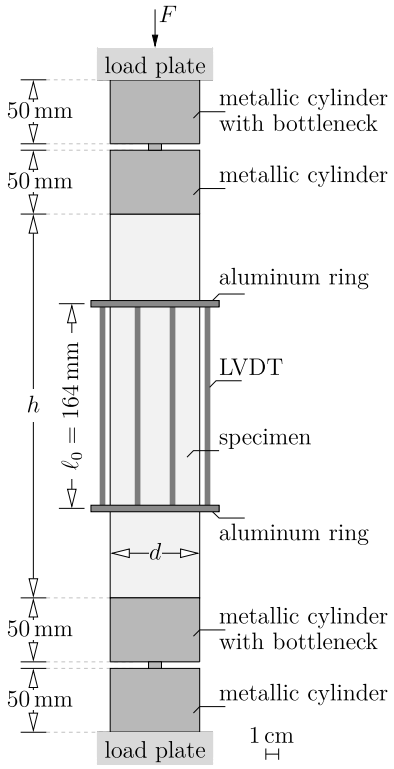


**Fig. 5.** Setup for hourly three-minute creep testing.

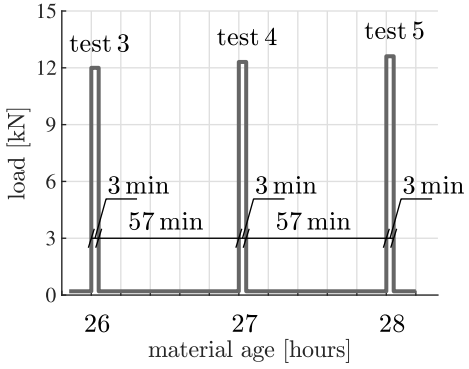


**Fig. 6.** History of loading prescribed in three consecutive creep tests performed at step-wisely increasing load levels; the diagram specifically shows data from tests 3, 4, and 5 of sample 1 of the OPC paste.

according to Eq. (8) with a nominal force rate of 3.85 kN/s, referring to a nominal stress rate of 1 MPa/s. The permanent load is kept constant for 57 min. The force, the shortening of the specimen between the two aluminum rings, and the temperature are measured, from 10 s before loading to 180 s after unloading, with a data acquisition rate of 100 Hz.

### 2.7. Time variables resolving the material age and the creep tests

The material age is resolved by means of the variable $t$. It runs from 0 to 168 h and resolves the first seven days after material production. The particular material age during the $k^{\text{th}}$ three-minute creep test is denoted by

$$t_k = 24\ \text{h} + \big[k-1\big] \times 1\ \text{h}\,, \tag{10}$$

where "h" stands for the physical unit "hour", and with

$$k = 1, 2, \dots, 145\,. \tag{11}$$

The creep tests are resolved by means of the variable $\tau$. It runs from 0 to 365 s and resolves the load application phase, the three-minute load plateau, the unloading phase, and some three minutes after unloading. Specific time instants at which readings of measurement sensors were captured are denoted as

$$\tau_j = j \times 0.01\ \text{s}\,, \tag{12}$$

where "s" stands for the physical unit "second", and with

$$j = 0, 1, 2, \dots, n\,, \tag{13}$$

as well as

$$n = 36500\,. \tag{14}$$

### 2.8. Quantification of shrinkage based on measured strains

Effective shrinkage (index *shr*) is quantified once every hour and relative to the situation right before the first creep test:

$$\varepsilon_{shr}(t_k) = \frac{1}{6}\sum_{i=1}^{6} \frac{u_i(t_k, \tau=0) - u_i(t_1, \tau=0)}{\ell_0}\,, \tag{15}$$

where $u_i$ stands for the length change measured by the $i^{\text{th}}$ sensor, with $i \in 1, 2, \dots, 6$. The six values $u_i(t_1, \tau=0)$ and the six values $u_i(t_k, \tau=0)$ refer to displacement measurements recorded right before the loading phases of the first creep test and of the $k^{\text{th}}$ creep test, respectively.

Effective shrinkage according to Eq. (15) includes hydration-induced shrinkage (historically referred to as "autogenous shrinkage" [37] and more recently as "self-desiccation shrinkage" [38]), unrecovered creep strains from previous creep tests, ongoing creep due to the small permanent force imposed on the specimen, and possibly drying shrinkage due to slightly imperfect sealing of the specimens. For the sake of brevity, effective shrinkage will be simply referred to as shrinkage in the following.

To quantify the shrinkage rate during the $k^{\text{th}}$ creep test, the shrinkage strains measured at the beginning of three consecutive creep tests, i.e. at material ages $t_{k-1}$, $t_k$, and $t_{k+1}$, are approximated by means of a quadratic polynomial, and its first derivative is evaluated at the central time instant $t_k$. This yields

$$\dot{\varepsilon}_{shr}(t_k) = \frac{\varepsilon_{shr}(t_{k+1}) - \varepsilon_{shr}(t_{k-1})}{t_{k+1} - t_{k-1}}\,, \tag{16}$$

where

$$t_{k+1} - t_{k-1} = 2 \times 3600\ \text{s}\,. \tag{17}$$

The shrinkage rate according to Eq. (16) is virtually constant throughout the short duration of the $k^{\text{th}}$ creep test. Thus, the evolution of shrinkage during every test, quantified relative to the situation at the start of the creep test, is virtually linear and reads as

$$\varepsilon_{shr}(t_k, \tau) = \dot{\varepsilon}_{shr}(t_k) \times \tau\,. \tag{18}$$

### 2.9. Identification of viscoelastic properties based on measured stresses and strains

An advanced protocol for the evaluation of hourly-performed three-minute creep tests is presented below. It is applicable to any cementitious material, because it contains two original features: (i) shrinkage strains are explicitly considered, and (ii) three viscoelastic quantities, i.e. the elastic modulus, the creep modulus, and the creep exponent, are robustly identified *without* making assumptions about any of these properties. The relations of these innovative features to the state-of-the-art will be discussed in Section 4.

As for the identification of viscoelastic properties, each three-minute creep test is evaluated individually. The stresses imposed on the specimen during testing are equal to the forces measured by the force cell of the testing machine, $F(t_k, \tau_j)$, divided by the cross-sectional area of the specimen, $A = d^2\pi/4$:

$$\sigma(t_k, \tau_j) = \frac{F(t_k, \tau_j)}{d^2\pi/4}\,, \tag{19}$$

with $\tau_j$ according to Eqs. (12)–(14). The strains developing in the central part of the specimen between the two aluminum rings are equal to the average of the length changes measured by the six displacement sensors divided by the initial distance between the two aluminum rings, see Eq. (9),

$$\varepsilon_{exp}(t_k, \tau_j) = \frac{1}{6}\sum_{i=1}^{6}\frac{u_i(t_k, \tau_j) - u_i(t_k, \tau=0)}{\ell_0}\,. \tag{20}$$

These strains contain contributions from the viscoelastic behavior induced by the $k^{\text{th}}$ test and from shrinkage. The viscoelastic strains (index *vel*) are obtained by subtracting the shrinkage strains according to Eq. (18) from the total strains according to Eq. (20):

$$\varepsilon_{vel}(t_k, \tau_j) = \varepsilon_{exp}(t_k, \tau_j) - \varepsilon_{shr}(t_k, \tau_j)\,. \tag{21}$$

To keep the nomenclature reasonably simple, the age of the material at the time of testing, $t_k$ according to Eq. (10), is omitted in the following.

The linear theory of viscoelasticity [39] is used to evaluate the stresses and strains of Eqs. (19) and (21). The corresponding integro-differential equation of hereditary mechanics, also referred to as "Boltzmann's superposition principle", provides access to the modeled strain history $\varepsilon_{mod}(\tau)$ as [40–42]

$$\varepsilon_{mod}(\tau) = \int_{-\infty}^{\tau} J(\tau-\theta)\,\frac{\mathrm{d}\sigma(\theta)}{\mathrm{d}\theta}\,\mathrm{d}\theta\,, \tag{22}$$

where $J$ is the creep function, $\mathrm{d}\sigma(\theta)/\mathrm{d}\theta$ is the stress rate history, and $\theta$ is an auxiliary time variable.

A power law is an appropriate creep function for modeling creep of cementitious materials with a characteristic duration from a few seconds to a few weeks [20,22,43–45]:

$$J(\tau-\theta) = \frac{1}{E} + \frac{1}{E_c}\left[\frac{\tau-\theta}{\tau_{ref}}\right]^{\beta}\,, \tag{23}$$

where $E$, $E_c$, and $\beta$ stand for the elastic modulus, the creep modulus, and the creep exponent, respectively. The reference time, $\tau_{ref}$, renders the argument inside the brackets of Eq. (23) dimensionless. It is set equal to 86400 seconds (= 1 day), following the example of [20,26].

The stress rate history is represented as a piece-wise constant function of time, using the Heaviside step function with $H(\theta \geq \tau_i) = 1$ and $H(\theta < \tau_i) = 0$:

$$\frac{\mathrm{d}\sigma(\theta)}{\mathrm{d}\theta} = \sum_{i=1}^{4}\dot{\sigma}_i\,H(\theta-\tau_i)\,, \tag{24}$$

see Fig. 7. Load application starts at time instant $\tau_1 = 0$ s, at stress rate $\dot{\sigma}_1 = \text{const}$. At time instant $\tau_2$, the load application ends and the load plateau starts. The vanishing stress rate during the load plateau is described by means of $\dot{\sigma}_2 = -\dot{\sigma}_1 = \text{const}$. At time instant $\tau_3$, the load plateau ends and the unloading starts at stress rate $\dot{\sigma}_3 = \text{const}$. At time instant $\tau_4$, the unloading ends and the phase of creep recovery starts. The vanishing stress rate after completed unloading is described by means of $\dot{\sigma}_4 = -\dot{\sigma}_3 = \text{const}$. Quantification of $\dot{\sigma}_1$, $\dot{\sigma}_3$, and $\tau_1$, $\tau_2$, $\tau_3$, and $\tau_4$ is explained in Appendix A.

Modeled strains follow from inserting Eqs. (23) and (24) into Eq. (22) and from solving the integral as

$$\varepsilon_{mod}(E, E_c, \beta; \tau) = \sum_{i=1}^{4}\frac{\dot{\sigma}_i\,\langle\tau-\tau_i\rangle}{E} + \frac{\dot{\sigma}_i\,\tau_{ref}}{E_c\,(\beta+1)}\left[\frac{\langle\tau-\tau_i\rangle}{\tau_{ref}}\right]^{\beta+1}\,, \tag{25}$$

where

$$\langle\tau-\tau_i\rangle = \left[\tau-\tau_i\right]\times H(\tau-\tau_i)\,. \tag{26}$$

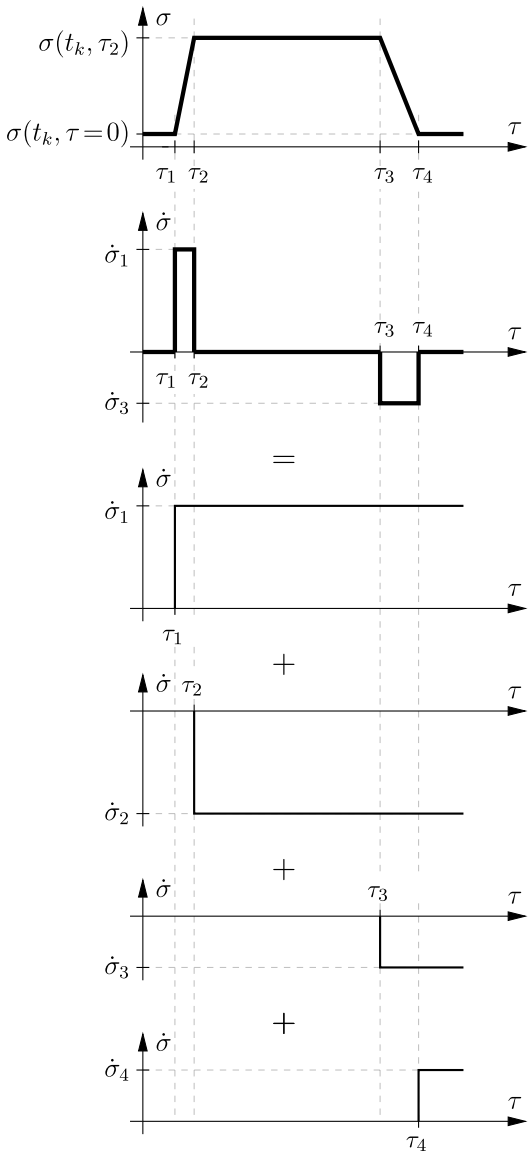


**Fig. 7.** Stress history used for the evaluation of three-minute creep tests, see the top diagram; the second diagram shows the corresponding stress *rate* history which can be decomposed into four stress rate steps, see the four bottom-most diagrams and Eq. (24).

The goal of the test evaluation is to find values of $E$, $E_c$, and $\beta$ such that the modeled strain history according to Eq. (25) best reproduces the viscoelastic strain history according to Eq. (21). This task is accomplished in two newly proposed steps. The first refers to the identification of $E_c$ and $\beta$. The second step refers to the identification of $E$.

**Step 1:** $E_c$ and $\beta$ are identified such that the modeled strains run as parallel as possible to the viscoelastic strains during the three-minute load plateau. The elastic modulus is set infinitely large ($E = \infty$), such that modeled strains contain creep strains only, see Fig. 8. Mathematically, the identification task is formulated as an optimization problem

$$\mathcal{E}(E_c, \beta) = \sqrt{\frac{1}{m}\sum_{j=1}^{m}\left[D(E_c, \beta; \tau_j) - \overline{D}(E_c, \beta)\right]^2} \;\rightarrow\; \min\,, \tag{27}$$

with

$$D(E_c, \beta; \tau_j) = \varepsilon_{mod}(E=\infty, E_c, \beta; \tau_j) - \varepsilon_{vel}(\tau_j)\,, \tag{28}$$

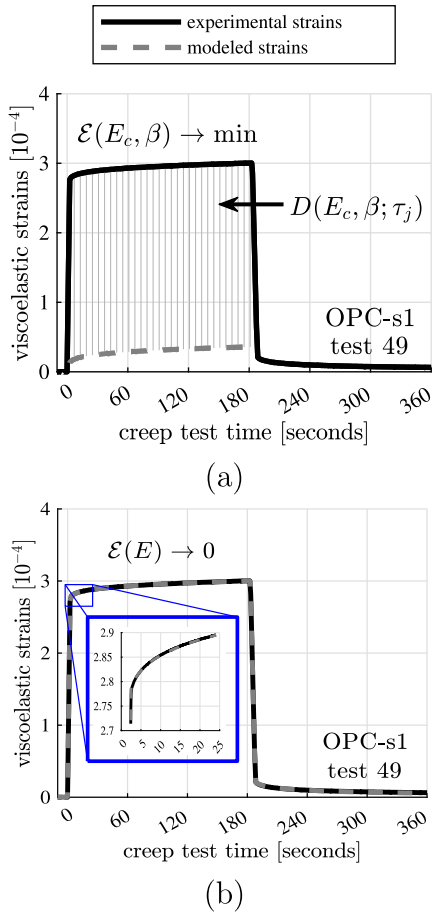


**Fig. 8.** Identification of viscoelastic properties: (a) Step 1: identification of the creep modulus $E_c$ and the creep exponent $\beta$ according to Eqs. (27)–(31) such that the modeled strains run as parallel as possible to the viscoelastic experimental strains during the three-minute load plateau; (b) Step 2: identification of the elastic modulus $E$ such that the mean difference between modeled and viscoelastic experimental strains vanishes during the three-minute load plateau, see Eq. (33); illustration for test 49 on OPC paste sample 1, performed at the material age of 72 h.

$$\overline{D}(E_c, \beta) = \frac{1}{m} \sum_{j=1}^{m} D(E_c, \beta; \tau_j), \tag{29}$$

and with

$$\tau_j = \tau_I + j \times 0.01 \text{ s}, \quad \forall\ j = 0, 1, 2, \ldots, m, \tag{30}$$

$$m = \frac{\tau_{II} - \tau_I}{0.01 \text{ s}}, \tag{31}$$

where $\tau_I$ and $\tau_{II}$ refer to the first and the last time instant, respectively, at which the measured stress was equal to (or slightly larger than) the average stress of the load plateau, see Appendix B for details.

The optimization starts with defining search intervals, e.g. $E_c \in [10\text{ GPa}, 100\text{ GPa}]$ and $\beta \in [0.1, 0.5]$. Both of them are discretized into 7 equidistant values. Combining 7 values of $E_c$ with 7 values of $\beta$ yields 49 pairs of values. Modeled strains are computed for each of these pairs according to Eq. (25), and the error function according to Eqs. (27)–(31) is evaluated. The specific pair of values of $E_c$ and $\beta$, which yields the smallest error, is treated as a near-optimal solution. A new iteration step is started. To define new search intervals, the ones previously used are either shifted, provided that the near-optimal solution is at the limit of the previous search interval, or refined, see [20] for details. The iteration is stopped once the search intervals are so small that all seven values of the search interval have the same first four significant digits. The pair of values delivering the smallest error according to Eqs. (27)–(31) at the end of the last iteration step is treated as the optimal solution. The identified values of $E_c$ and $\beta$ are denoted as $E_c^*$ and $\beta^*$. They are kept constant throughout the following step 2, during which the value of the elastic modulus is identified.

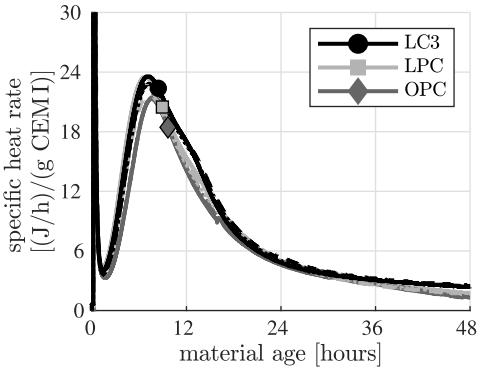


**Fig. 9.** Calorimetry results: heat release rate, normalized to the initial mass of the CEM I contained in the binder (see Table 1), as a function of material age; symbols are provided for better readability; differences between the three tested materials are clearly visible in the cumulative heat evolutions of Fig. 10.

**Step 2:** $E$ is identified such that the mean difference between modeled and viscoelastic experimental strains vanishes during the three-minute load plateau:

$$\mathcal{E}(E) = \frac{1}{m} \sum_{j=1}^{m} \left[ \varepsilon_{mod}(E, E_c^*, \beta^*; \tau_j) - \varepsilon_{vel}(\tau_j) \right] \rightarrow 0\,. \tag{32}$$

The solution of Eq. (32) reads as

$$E^* = \left| \frac{\overline{D}(E_c^*, \beta^*)}{\dot{\sigma}_1 \left[\tau_2 - \tau_1\right]} \right|, \tag{33}$$

where $\dot{\sigma}_1 \left[\tau_2 - \tau_1\right]$ denotes the stress increment imposed on the specimen during load application.

In order to assess the significance of the identified values of $E^*$, $E_c^*$, and $\beta^*$, the root mean square error between modeled and viscoelastic experimental strains is quantified during the *entire* time interval from the start of the loading phase to 180 s after completed unloading,

$$\mathcal{E}(E^*, E_c^*, \beta^*) = \sqrt{\frac{1}{n} \sum_{j=1}^{n} \left[ \varepsilon_{mod}(E^*, E_c^*, \beta^*; \tau_j) - \varepsilon_{vel}(\tau_j) \right]^2}, \tag{34}$$

with $\tau_j$ and $n$ according to Eqs. (12)–(14).

In order to verify the robustness of the described identification procedure, it was repeated several times, starting from *different* initial search intervals for $E_c$ and $\beta$, for each one of the here described 870 three-minute creep tests. The results obtained were always very similar. This underlines that they are virtually independent of the initial search intervals.

## 3. Experimental results

### 3.1. Hydration kinetics

The heat release rate obtained from quasi-isothermal differential calorimetry is normalized with respect to the initial mass of the CEM I contained in the binder, see Table 1. Three nominally identical tests per material are represented by separated graphs in Fig. 9. The experimental dispersion is small. Test repeatability is satisfactory.

The acceleration period of both the LPC and LC3 pastes starts some 1 h and 25 min after material production. That of the OPC paste follows some 25 min later. The main peak of hydration is reached some seven hours after production of the LPC and LC3 pastes. That of the OPC paste follows some 45 min later. The LC3 paste shows the largest peak value of the specific heat release rate. The OPC paste shows the smallest peak

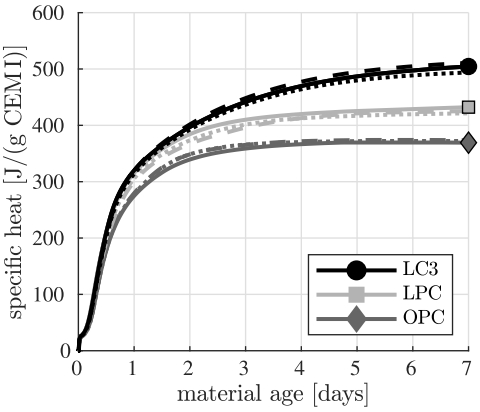


**Fig. 10.** Calorimetry results: cumulative heat release, normalized to the initial mass of the CEM I contained in the binder (see Table 1), as a function of material age; ordinate values are computed by inserting data from Fig. 9 into Eq. (1); symbols are provided for better readability.

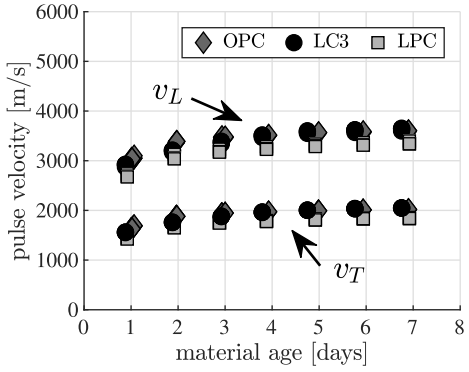


**Fig. 11.** Ultrasonic testing results: longitudinal ($v_L$) and transversal ($v_T$) ultrasonic wave velocities as a function of material age; ordinate values are computed by means of Eqs. (2) and (3).

value. That of the LPC paste is in between. After the main hydration peak, a characteristic "shoulder" illustrates that the aluminate reactions contribute measurably to the hydration reactions. This shoulder is more pronounced for the LC3 paste than for the OPC and LPC pastes, because of the larger aluminum content [46].

The evolution of the cumulative specific heat is obtained from inserting the data of Fig. 9 into Eq. (1), see Fig. 10. Already 12 h after material production, the LC3 paste shows the largest values of the cumulative heat release per initial mass of cement. The OPC paste shows the smallest values. Those of the LPC paste are in between. The hydration of the LPC paste is accelerated relative to the hydration of the OPC paste, because the limestone particles provide preferred nucleation sites for the growth of C-S-H [47–49]. The LC3 paste initially shows a similar behavior as the LPC paste. The LC3 paste exhibits a significantly larger heat release than the LPC paste, from a material age of 2 days onward, indicating the pozzolanic reaction which is a characteristic part of LC3 hydration [8,50].

### 3.2. Evolution of ultrasonics-derived elastic stiffness

Three cylindrical specimens of each of the three materials were tested. Their heights amount to $60.0 \pm 0.3$ mm. Their diameters amount to $29.4 \pm 1.2$ mm. The measured times of flight and delay times are converted by means of Eqs. (2) and (3) to longitudinal and transversal wave velocities, see Fig. 11.

The elastic modulus is quantified by means of evaluating Eqs. (4)–(6) for the wave velocities from Fig. 11 and the mass densities of the tested materials from Table 5, see Fig. 12. The elastic stiffness of all three materials increases monotonically with increasing material age. The elastic modulus of the LPC paste is virtually 25% smaller than that of the OPC paste, during the testing period from 1 to 7 days after material production. This is consistent with results presented in [51] where LPC systems with clinker replacement ratios up to 45% showed an elastic stiffness which was by up to 33% smaller than that of the OPC reference. At a material age of 1 day, the elastic stiffness of the LC3 paste is in between those of the LPC and OPC pastes. Subsequently, the stiffness increase of the LC3 paste is larger than that of the OPC paste, such that both materials have virtually the same stiffness some 6 days after material production. The results of Fig. 12 will be used for validation of the elastic moduli identified from hourly three-minute creep testing, see Section 3.7.

**Table 5**
Mass densities of the tested materials.

| Material | Mass density |
|---|---|
| OPC paste | $1.89 \pm 0.01$ g/cm$^3$ |
| LPC paste | $1.85 \pm 0.01$ g/cm$^3$ |
| LC3 paste | $1.85 \pm 0.01$ g/cm$^3$ |

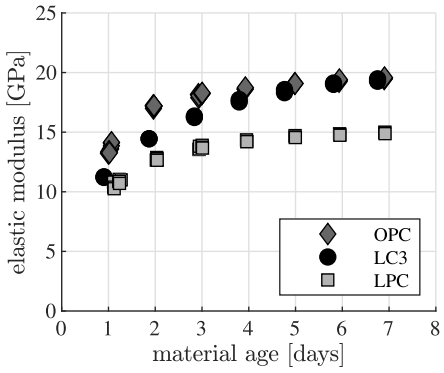


**Fig. 12.** Ultrasonic testing results: elastic moduli as a function of material age.

### 3.3. Evolution of uniaxial compressive strength

The maximum force recorded in the destructive uniaxial compression tests and the cross-sectional area of the specimens ($A = 6.80 \pm 0.06$ cm$^2$) are converted by means of Eq. (7) into the uniaxial compressive strength, see Fig. 13. The uniaxial compressive strength of all three materials increases monotonically with increasing material age. 7 days after material production, the compressive strength of the LC3 and LPC pastes amounts to about 81% and 57% of that of the OPC paste, respectively.

Prescribing 15% of the strength during every three-minute creep test requires a continuous mathematical description of the strength evolution. To this end, a power-law is introduced:

$$f_c(t) = a \left[ \frac{t}{1 \text{ day}} \right]^b . \tag{35}$$

The parameters $a$ and $b$ are optimized using the curve fitting tool of MatLab, see Table 6 for the results. The coefficients of determination, $R^2$, range from 92.6% to 97.5%, see Table 6. The fitted power laws slightly underestimate the strength of the OPC and LC3 pastes 3 days after production. Thus, the compressive loads prescribed during three-minute creep testing are even slightly smaller than 15% of the actual material strength. This underlines that the materials remained undamaged throughout the creep testing campaign.

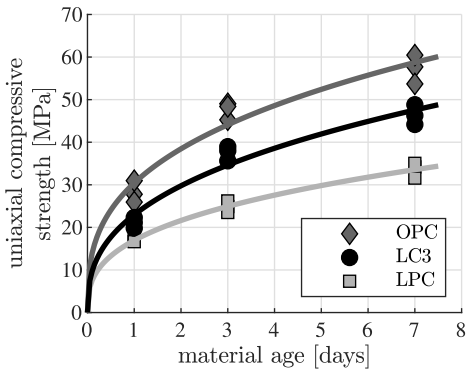


**Fig. 13.** Evolution of the uniaxial compressive strength as a function of material age: symbols label experimental results; the solid lines show the power law of Eq. (35) with parameters of Table 6.

**Table 6**
Values of parameters according to Eq. (35), allowing for the reproduction of experimentally obtained strength values.

| Material | $a$ | $b$ | $R^2$ |
|---|---|---|---|
| OPC paste | 30.42 MPa | 0.338 | 0.926 |
| LPC paste | 16.95 MPa | 0.351 | 0.975 |
| LC3 paste | 22.97 MPa | 0.374 | 0.941 |

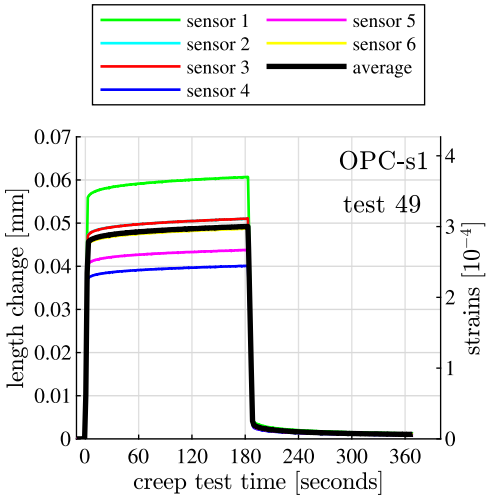


**Fig. 14.** Result of a three-minute creep test: the change of distance between two aluminum rings clamped to the specimen, measured by means of six displacement sensors; the differences of the sensor measurements result from eccentric loading by 1.2 mm which is significantly smaller than the diameter of the specimen (= 70 mm); illustration for test 49 on OPC paste sample 1, performed at the material age of 72 h. (For interpretation of the references to color in this figure legend, the reader is referred to the web version of this article.).

### 3.4. Length changes and strains measured during individual creep tests

The length changes measured by the six displacement sensors during one three-minute creep test show a parallel evolution, see e.g. Fig. 14. The differences result from the slightly eccentric application of the load. The load eccentricity, i.e. the lateral distance between the axis of loading and the axis of the specimen, is exemplarily quantified for the test shown in Fig. 14. Following Eqs. (3)–(6) of [32], the eccentricity amounts to some 1.2 mm. This is a very small and therefore tolerable eccentricity, when compared with 70 mm (= the nominal diameter of the specimens).

The average of the six measurements delivers the average shortening of the measured part of the specimen, see the black line in Fig. 14.

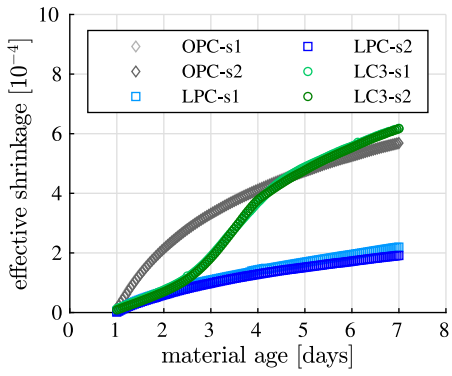


**Fig. 15.** Result of hourly three-minute creep testing: effective shrinkage of OPC, LPC, and LC3 pastes as a function of material age; effective shrinkage includes hydration-induced shrinkage, unrecovered creep strains from previous creep tests, ongoing creep due to the small permanent force imposed on the specimen, and possibly drying shrinkage due to slightly imperfect sealing of the specimens.

Experimental strains are quantified by means of Eq. (20), see also the right ordinate in Fig. 14.

### 3.5. Shrinkage of specimens subjected to creep testing

Shrinkage strains quantified for all three tested materials according to Eq. (15) increase monotonically with increasing material age, see Fig. 15. Test repeatability is satisfactory, noting the small experimental variation obtained with two nominally identical samples of each one of the three tested materials. The shrinkage curves of the OPC and LPC pastes show a negative curvature. That of the LC3 paste starts with a positive curvature, shows an inflection point about 3.5 days after material production, and then shows a negative curvature. These results will be discussed in Section 5.2.

### 3.6. Creep-testing-derived evolution of elastic stiffness and creep

The elastic modulus, the creep modulus, and the creep exponent are quantified according to Eqs. (19)–(33), using the actual dimensions of the specimens. Their heights amount to 30.00 cm ± 0.01 cm and their diameters to 7.08 cm ± 0.03 cm, respectively. The minimum duration of the load application phase amounts to 1.2 s and refers to test 1 of the LPC paste. Thus, the minimum duration of the unloading phase amounts to 2.4 s. The maximum duration of the load application phase amounts to 4.2 s and refers to test 145 of the OPC paste. Thus, the maximum duration of the unloading phase amounts to 8.4 s.

The elastic modulus increases monotonically with increasing material age for all three tested materials, see Fig. 16(a). The results are reminiscent of the ones obtained from ultrasonic testing. For the direct comparison of Figs. 12 and 16(a) see Section 3.7.

The creep modulus of all three materials increases monotonically with increasing material age, see Fig. 16(b). The creep modulus of the OPC paste is larger than that of the LPC paste throughout the creep testing campaign from 1 to 7 days. During the first 3 days, the creep modulus of the LC3 paste evolves in a very similar way to that of the LPC paste. Thereafter, the creep modulus of the LC3 paste increases faster than that of the OPC paste, such that the LC3 paste has the largest creep modulus among all three tested materials from some 4 days after production.

The creep exponent of all three materials decreases monotonically with increasing material age, see Fig. 16(c). The creep exponent of the OPC paste is larger than that of the LPC paste throughout the creep testing campaign. Notably, the creep exponent evolutions of the OPC and LPC pastes show a positive curvature, while that of the LC3 paste shows two inflection points.

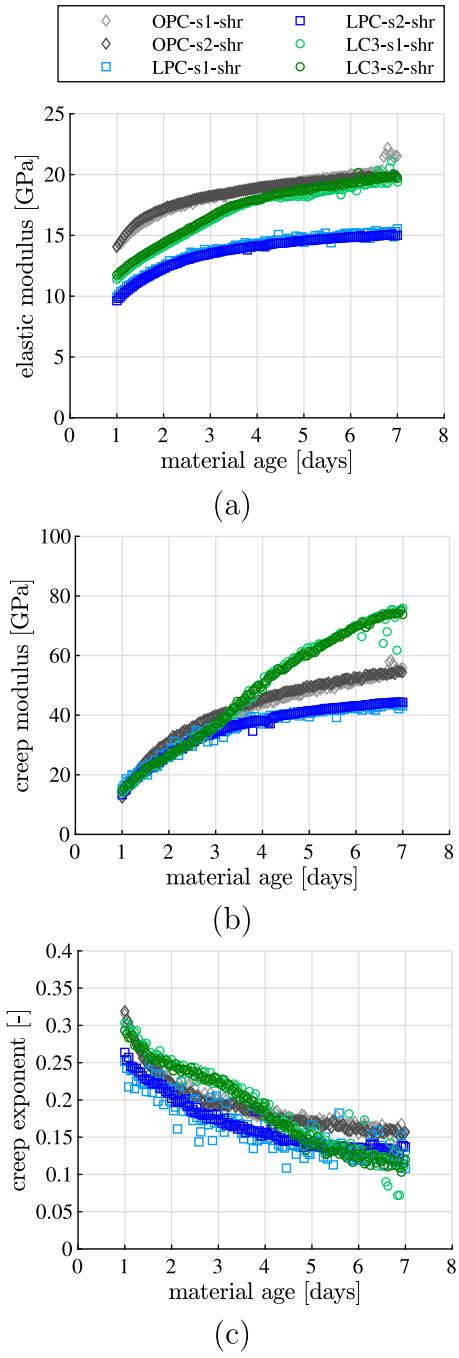


**Fig. 16.** Hourly performed three-minute creep testing results: (a) elastic modulus $E^*$, (b) creep modulus $E_c^*$, and (c) creep exponent $\beta^*$ as functions of the material age.

The interpretation of the creep modulus and the creep exponent is the topic of Section 4.7. The corresponding discussion of the experimental results illustrated in Fig. 16(b) and (c) is provided in Section 5.4. Here, it is worth mentioning that the root mean square errors between modeled and experimental strains according to Eq. (34) are, except for single outliers, smaller than $1.5 \times 10^{-6}$, see Fig. 17. These values are by three orders of magnitude smaller than the characteristic strains measured during the three-minute load plateau, see e.g. the right ordinate in Fig. 14. This underlines the very satisfactory accuracy with which the modeling approach reproduces the viscoelastic strains.

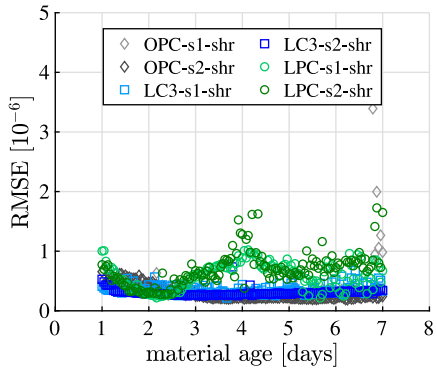


**Fig. 17.** Root mean square errors (RMSE) between modeled and viscoelastic experimental strains, quantified according to Eq. (34) for every three-minute creep test, under consideration of shrinkage strains according to Eq. (15).

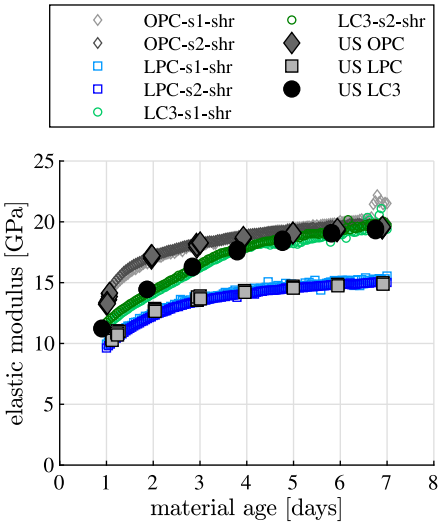


**Fig. 18.** Comparison of the elastic stiffness evolutions obtained from ultrasonic testing, see Fig. 12, and from creep testing, see Fig. 16(a).

### *3.7. Comparison of the elastic stiffness evolutions obtained from ultrasonic and creep testing*

The ultrasonic tests, see Fig. 12, and the creep tests, see Fig. 16(a), provide independent access to the evolution of the elastic modulus of the three tested materials. Illustrating the results of both characterization methods in one diagram underscores that virtually the same stiffness evolutions are obtained, Thus, both methods mutually corroborate each other, see Fig. 18.

## 4. Discussion of the test evaluation protocol and of the associated strain modeling approach

### *4.1. Differences between existing test evaluation strategies and the here-proposed protocol*

Herein, a further improved strategy for the evaluation of three-minute creep tests was presented. It is the successor of two preceding test evaluation strategies.

Irfan-ul-Hassan et al. [20] used a two-step strategy. In step 1, the elastic modulus was estimated based on the unloading modulus and improved such as to avoid modeling of nonphysical tensile creep strains at the very beginning of the load application phase. In step 2, the creep modulus and the creep exponent were identified such as to minimize

the differences between modeled and measured strains during both the load application phase and the subsequent 180 s of constant loading.

Ausweger et al. [26] set the creep exponent equal to 0.25. This was motivated by a multiscale continuum micromechanics model for non-aging basic creep of ordinary Portland cement pastes [22]. Therein, the microstructure of cement paste was resolved down to capillary pores and microscopic hydrate gel needles. Their isochoric creep behavior was described by means of a creep shear modulus and a creep exponent. The values of these two material *constants* were identified such as to best reproduce the macroscopic creep behavior of ordinary Portland cement pastes with initial water-to-cement mass ratios amounting to 0.42, 0.45, and 0.50, measured in some 500 three-minute creep tests performed at material ages from 1 to 8 days [20]. The identified hydrate gel needle-related creep exponent amounts to 0.25. Upscaling by means of the multiscale model delivered the corresponding macroscopic creep exponent of cement paste, which was also equal to 0.25.[1] This value was taken over by Ausweger et al. [26] who used a single-step strategy for the identification of the elastic modulus and the creep modulus, such as to minimize the differences between modeled and measured strains both during the load application phase and the subsequent 180 s of constant loading.

Herein, a new two-step strategy for the evaluation of three-minute creep tests was used. In step 1, the creep modulus and the creep exponent are identified to maximize the parallelism between modeled and measured strains during the 180 s of constant loading. In step 2, the elastic modulus is identified such that the mean difference between modeled and experimental strains vanishes during the 180 s of constant loading. This approach was the result of the following arguments:

- The creep exponent is constant during individual three-minute tests, but it is allowed to vary from one test to another. The underlying rational is twofold. (i) Since the creep behavior of the LC3 paste is unknown, it would be unjustified to assume that the creep exponent has always the same value. (ii) All creep tests of all three materials shall be identified by means of *the same method* to ensure comparability of the results.
- Identification of the *creep* modulus and the *creep* exponent was based on strains measured during the 180 s of constant loading.[2] The underlying rational is that the viscoelastic strain increases *during* the load plateau exclusively due to *creep*, because the elastic deformation is constant.
- The identification of the elastic modulus was also based on strains measured during the 180 s of constant loading. The quality of the identification results was quantified by means of the root mean square error evaluated during the *entire* time interval from the start of the load application to some 180 s after completed unloading, see Eq. (34). This assessment is meaningful, given that strains measured during the phases of load application, unloading, and creep recovery had to be *predicted*, as they were not used as input for the preceding identification task.

Another innovative aspect of the here-proposed test evaluation strategy is that identification of *viscoelastic* material properties was based on *viscoelastic strains* which were quantified by subtracting shrinkage strains from measured strains. Notably, *measured strains* were used as input for the identification of viscoelastic material properties in the two preceding test evaluation strategies [20,26]. This provides the motivation to discuss the significance of shrinkage strains in the following two Subsections.

[1] The equality of microscopic and macroscopic creep exponents is a result of inefficient stress redistribution from creeping hydrate gel needles to purely elastic (*non-creeping*) cement grains [29].

[2] Still, creep strains developing during the short phase of fast load application were also included in the modeling approach.

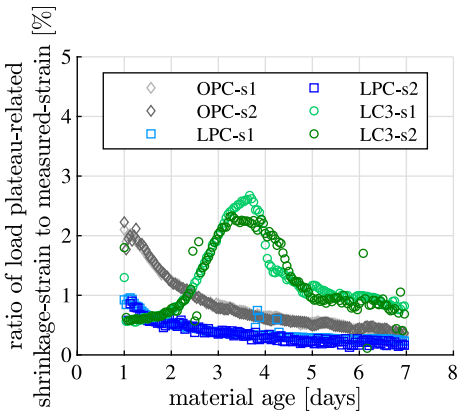


**Fig. 19.** Ratio between shrinkage increments and total strain increments measured during three-minute load plateaus of individual creep tests, as a function of material age.

### 4.2. Contribution of shrinkage to strains measured during load plateaus

The load plateau-related ratio of the shrinkage-strain-increment and the measured-strain-increment reads, for the $k^{\text{th}}$ creep test, as:

$$\mathcal{I}(t_k) = \frac{\dot{\varepsilon}_{shr}(t_k) \times \left[\tau_3 - \tau_2\right]}{\varepsilon_{exp}(t_k, \tau_3) - \varepsilon_{exp}(t_k, \tau_2)} \,. \tag{36}$$

Eq. (36) expresses that the increment of shrinkage strains developing during the load plateau is equal to the shrinkage rate multiplied with the duration of the load plateau, see the numerator of Eq. (36). The increment of measured strains developing during the load plateau is equal to the difference of the strains measured at the end and at the start of the load plateau, see the denominator of Eq. (36).

Eq. (36) is evaluated for all six tested specimens and for all three-minute creep tests, except the first and the last tests for which the shrinkage rate $\dot{\varepsilon}_{shr}(t_k)$ according to Eq. (16) cannot be evaluated. The obtained values of the load plateau-related ratio of shrinkage-strain increments and measured-strain increments are smaller than 3%, see Fig. 19. The largest values are obtained for the LC3 paste during the fourth day after production, see the green symbols in Fig. 19. Notably, the steeper the slope of the shrinkage strain evolution in Fig. 15, the larger is the ratio in Fig. 19. This underlines that shrinkage does contribute to the strains measured during a three-minute creep test. The fact that shrinkage was disregarded in the preceding test evaluation strategies [20,24,26,29] provides the motivation for the next subsection.

### 4.3. Identification of viscoelastic properties from measured rather than viscoelastic strains

Herein, identification of $E$, $E_c$, and $\beta$ is repeated for all three-minute creep tests. This time, modeled strains shall reproduce the *measured* strains. Therefore, the viscoelastic strains $\varepsilon_{vel}(\tau_j)$ are replaced by the measured strains $\varepsilon_{exp}(\tau_j)$ in Eqs. (28) and (32). This yields:

$$D(E_c, \beta; \tau_j) = \varepsilon_{mod}(E_c, \beta; \tau_j) - \varepsilon_{exp}(\tau_j) \tag{37}$$

and

$$\mathcal{E}(E) = \frac{1}{m} \sum_{j=1}^{m} \left[ \varepsilon_{mod}(E, E_c, \beta; \tau_j) - \varepsilon_{exp}(\tau_j) \right] \rightarrow 0 \,. \tag{38}$$

All other Eqs. (27)–(33) remain the same. Solving the modified minimization problem yields newly identified values of $E$, $E_c$, and $\beta$, referred to as $E^\star$, $E_c^\star$, and $\beta^\star$. The corresponding root mean square error follows from replacing $\varepsilon_{vel}(\tau_j)$ in Eq. (34) by $\varepsilon_{exp}(\tau_j)$:

$$\mathcal{E}(E^\star, E_c^\star, \beta^\star) = \sqrt{\frac{1}{n} \sum_{j=1}^{n} \left[ \varepsilon_{mod}(E^\star, E_c^\star, \beta^\star; \tau_j) - \varepsilon_{exp}(\tau_j) \right]^2} \,. \tag{39}$$

**Table 7**
Comparison of root mean square errors between modeled and experimentally quantified strains, which are averaged over all 145 tests per specimen according to two different test evaluation strategies: $\text{avg}\left[\mathcal{E}(\varepsilon_{mod}-\varepsilon_{vel})\right]$ refers to identification of viscoelastic properties from viscoelastic strains, see Section 2.9; $\text{avg}\left[\mathcal{E}(\varepsilon_{mod}-\varepsilon_{exp})\right]$ refers to identification of viscoelastic properties from measured strains.

| | $\text{avg}\left[\mathcal{E}(\varepsilon_{mod}-\varepsilon_{vel})\right]$ | $\text{avg}\left[\mathcal{E}(\varepsilon_{mod}-\varepsilon_{exp})\right]$ |
|---|---|---|
| OPC-s1 | $0.30\times10^{-6}$ | $0.37\times10^{-6}$ |
| OPC-s2 | $0.61\times10^{-6}$ | $0.67\times10^{-6}$ |
| LPC-s1 | $0.36\times10^{-6}$ | $0.36\times10^{-6}$ |
| LPC-s2 | $0.30\times10^{-6}$ | $0.31\times10^{-6}$ |
| LC3-s1 | $0.76\times10^{-6}$ | $0.85\times10^{-6}$ |
| LC3-s2 | $0.59\times10^{-6}$ | $0.69\times10^{-6}$ |

Identifying viscoelastic properties either from *viscoelastic* strains, see Section 2.9 and Fig. 16, or from *measured* strains, see above and Fig. C.29, yields very similar results in terms of the elastic modulus, the creep modulus, and the creep exponent. As for a quantitative comparison, the 145 values of the root mean square error, referring to the 145 tests per specimen, are averaged. Averaging over the errors according to Eqs. (34) and (39) yields quantities referred to as $\text{avg}\left[\mathcal{E}(\varepsilon_{mod}-\varepsilon_{vel})\right]$ and as $\text{avg}\left[\mathcal{E}(\varepsilon_{mod}-\varepsilon_{exp})\right]$, respectively, see Table 7. Identifying viscoelastic properties from *viscoelastic* strains yields average strain reproduction errors $\text{avg}\left[\mathcal{E}(\varepsilon_{mod}-\varepsilon_{vel})\right]$ which are smaller than the average strain reproduction errors $\text{avg}\left[\mathcal{E}(\varepsilon_{mod}-\varepsilon_{exp})\right]$ obtained when identifying viscoelastic properties from *measured* strains, see Table 7.

It is concluded that it is preferable to subtract shrinkage strains from measured strains in order to obtain viscoelastic strains and to use these viscoelastic strains for the identification of viscoelastic properties. It is also concluded that the alternative of identifying viscoelastic properties simply from measured strains, as done e.g. in [20,24,26,29], delivers also very meaningful results, because the contribution of shrinkage to measured strains is small, see Fig. 19.

### 4.4. Creep deformation during load application and load plateau

In the idealized scenario of infinitely fast loading, only elastic deformation develops during load application. In real testing, however, load application cannot be infinitely fast. This provides the motivation to quantify the creep deformation developing during load application. The strain at the end of the load application phase follows from evaluating Eq. (25) for $\tau=\tau_2$:

$$\varepsilon_{mod}(\tau)\Big|_{\tau=\tau_2} = \frac{\dot\sigma_1\left[\tau_2-\tau_1\right]}{E} + \frac{\dot\sigma_1\,\tau_{ref}}{E_c\left[\beta+1\right]}\left[\frac{\tau_2-\tau_1}{\tau_{ref}}\right]^{\beta+1}. \tag{40}$$

The first term on the right-hand-side of Eq. (40) refers to the elastic deformation, and the following term to creep deformation.

The strain at the end of the three-minute load plateau follows from evaluating Eq. (25) for $\tau=\tau_3$. Simplifying the obtained expression under consideration of $\dot\sigma_2=-\dot\sigma_1$ yields

$$\varepsilon_{mod}(\tau)\Big|_{\tau=\tau_3} = \frac{\dot\sigma_1\left[\tau_2-\tau_1\right]}{E} + \frac{\dot\sigma_1\,\tau_{ref}}{E_c\left[\beta+1\right]}\left\{\left[\frac{\tau_3-\tau_1}{\tau_{ref}}\right]^{\beta+1}-\left[\frac{\tau_3-\tau_2}{\tau_{ref}}\right]^{\beta+1}\right\}. \tag{41}$$

The first term on the right-hand-side of Eq. (41) refers to the elastic deformation, and the following term to creep deformation.

Dividing the creep deformation at the end of the load application phase according to Eq. (40) by the creep deformation at the end of the three-minute load plateau according to Eq. (41) delivers the portion of creep deformation developing during fast load application:

$$\mathcal{I}_{creep} = \frac{\left[\frac{\tau_2-\tau_1}{\tau_{ref}}\right]^{\beta+1}}{\left[\frac{\tau_3-\tau_1}{\tau_{ref}}\right]^{\beta+1}-\left[\frac{\tau_3-\tau_2}{\tau_{ref}}\right]^{\beta+1}}. \tag{42}$$

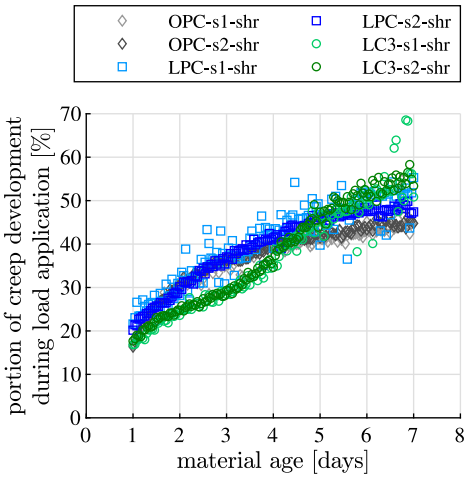


**Fig. 20.** Creep strains developing during the loading phase relative to creep strains developing up to the end of the load plateau.

Evaluation of Eq. (42) for all three-minute creep tests shows that some 20% to some 60% of the creep deformation developing until the end of the 180 s load plateau are already induced during the short phase of fast loading, see Fig. 20. On the one hand, this is a result of the short duration of the creep tests and the very steep initial slope of the creep function. On the other hand, the increasing trends in Fig. 20 are influenced by the fact that the speed of load application was always the same, while the level of the load plateau was increased from test to test. Thus, the load application phase of tests at higher material age lasted longer than those at lower material age, and a longer duration of the load application phase allowed the materials to develop more creep strains. Fig. 20 also implies that only some 40% to some 80% of the creep deformation develop during the three-minute load plateau. It is concluded that Eq. (42) and Fig. 20 underscore the importance of accounting for creep strains developing already during fast load application when it comes to the evaluation of a creep test with a characteristic duration of a few minutes or less.

*Disregarding* creep deformation developing during load application, i.e. treating the entire deformation measured during load application as elastic deformation, results in an overestimation of the elastic deformation and in an underestimation of the creep deformation. The incorrect estimation is the larger the smaller the speed of loading, i.e. the more time is provided for creep strains to develop during the load application. As for the here-used loading stress rate of 2 MPa/s, the misestimation of the elastic modulus and the creep modulus can be quantified as follows:

- The underestimation of the elastic modulus is rather moderate. It amounts to a few percent, because the elastic deformation developing during load application [see the first term on the right-hand-side of Eq. (40)] is significantly larger than the creep deformation developing during load application [see the last term of Eq. (40)], i.e.

$$\frac{\dot\sigma_1\left[\tau_2-\tau_1\right]}{E} \gg \frac{\dot\sigma_1\,\tau_{ref}}{E_c\left[\beta+1\right]}\left[\frac{\tau_2-\tau_1}{\tau_{ref}}\right]^{\beta+1}. \tag{43}$$

- The overestimation of the creep modulus is significant. It amounts to a multiplicative factor of up to 2.5, because the creep strain developing during load application [see the last term in Eq. (40)] is responsible for 20% to 60% of the creep deformation developing until the end of the 180 s load plateau [see the second line of Eq. (41)], i.e.

$$\left[\frac{\tau_2-\tau_1}{\tau_{ref}}\right]^{\beta+1} \ll \left[\frac{\tau_3-\tau_1}{\tau_{ref}}\right]^{\beta+1}-\left[\frac{\tau_3-\tau_2}{\tau_{ref}}\right]^{\beta+1}. \tag{44}$$

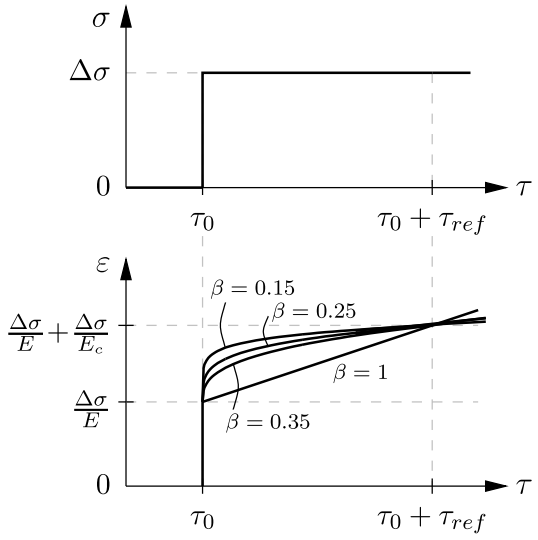


**Fig. 21.** Interpretation of the elastic modulus, the creep modulus, the creep exponent, and the reference time.

### 4.5. Mechanical interpretation of the creep modulus, the creep exponent, and the reference time

As for the interpretation of $E_c$, $\beta$, and $\tau_{ref}$, it is useful to consider an idealized scenario. It consists of imposing a uniaxial stress $\Delta\sigma$ *infinitely fast* at time $\tau_0$ on a material sample with a *chemically inert* microstructure, such that the same creep properties $E_c$ and $\beta$ remain valid even if the load plateau lasts for a time period of more than $\tau_{ref}$; note that $\tau_{ref} = 1$ day was used herein and in [20,26,29]. The imposed stress history reads as

$$\sigma(\tau) = \Delta\sigma\, H(\tau - \tau_0)\,, \tag{45}$$

see also Fig. 21. The corresponding stress rate history reads as

$$\frac{\mathrm{d}\sigma(\theta)}{\mathrm{d}\theta} = \Delta\sigma\, \delta(\theta - \tau_j)\,, \tag{46}$$

where $\delta(\theta - \tau_j)$ denotes the Dirac delta function. Inserting Eqs. (23) and (46) into Eq. (22), and solving the integral yields the strain history as

$$\varepsilon(\tau) = \left\{ \frac{\Delta\sigma}{E} + \frac{\Delta\sigma}{E_c} \left[ \frac{\tau - \tau_0}{\tau_{ref}} \right]^{\beta} \right\} H(\tau - \tau_0)\,, \tag{47}$$

see also Fig. 21.

The infinitely fast loading at the time $\tau_0$ does not provide a time span that is necessary for the creep deformation to develop. Thus, the material develops an elastic strain only. It amounts to the stress step divided by the elastic modulus:

$$\varepsilon(\tau)\Big|_{\tau=\tau_0^+} = \frac{\Delta\sigma}{E}\,, \tag{48}$$

see Fig. 21 and note that $\tau_0^+$ is equal to $\lim_{\epsilon\to 0}[\tau_0 + \epsilon]$.

At the time instant $\tau = \tau_0 + \tau_{ref}$, the term in the brackets of Eq. (47) is equal to 1. This implies:

$$\varepsilon(\tau)\Big|_{\tau=\tau_0+\tau_{ref}} = \frac{\Delta\sigma}{E} + \frac{\Delta\sigma}{E_c}\,, \tag{49}$$

see also Fig. 21. Eq. (48) clarifies that $1/E$ is the spontaneous elastic compliance of the material. Eq. (49) clarifies $1/E_c$ is the additional creep compliance, a time period of $\tau_{ref}$ after load application. It is concluded that the interpretation of the creep modulus depends on the chosen reference time. This will be further clarified in Section 4.6.

The value of the creep exponent $\beta$ determines the nonlinearity with which the creep strain develops in the interval from infinitely fast loading at time $\tau_0$ to the time instant $\tau_0 + \tau_{ref}$. The smaller the value of $\beta$, the larger the creep rate remains right after the load is applied, and the smaller the creep rate becomes when approaching the time instant $\tau_0 + \tau_{ref}$, and vice versa, see Fig. 21.

### 4.6. Robustness of the test evaluation protocol with respect to different choices of the reference time

The present Subsection refers to the effects of changing the reference time from $\tau_{ref} = 1$ day to any other positive value $\tau^\diamond_{ref}$. Repeating the identification of the viscoelastic properties yields corresponding values of the elastic modulus, the creep modulus, and the creep exponent referred to as $E^\diamond$, $E^\diamond_c$, and $\beta^\diamond$. Since the creep behavior of cement paste is independent of its mathematical description, the creep function described by means of $\tau_{ref}$, $E$, $E_c$, and $\beta$ must be identical to that described by means of $\tau^\diamond_{ref}$, $E^\diamond$, $E^\diamond_c$, and $\beta^\diamond$:

$$\frac{1}{E} + \frac{1}{E_c}\left[\frac{\tau - \tau_0}{\tau_{ref}}\right]^{\beta} = \frac{1}{E^\diamond} + \frac{1}{E^\diamond_c}\left[\frac{\tau - \tau_0}{\tau^\diamond_{ref}}\right]^{\beta^\diamond}\,. \tag{50}$$

Eq. (50) implies three conditions that must be fulfilled when replacing $\tau_{ref}$ by $\tau^\diamond_{ref}$

$$E = E^\diamond\,, \tag{51}$$

$$\beta = \beta^\diamond\,, \tag{52}$$

$$E_c\left[\tau_{ref}\right]^{\beta} = E^\diamond_c\left[\tau^\diamond_{ref}\right]^{\beta^\diamond}\,. \tag{53}$$

And indeed, replacing $\tau_{ref} = 86{,}400$ s (= 1 day) in Eq. (23) by $\tau^\diamond_{ref} = 180$ s (= 3 min) and repeating the creep test evaluation according to Eqs. (27)–(33) yields updated values of the elastic modulus, the creep modulus, and the creep exponent. The virtually perfect correlation plots between the elastic modulus, the creep modulus, and the creep exponent according to Fig. 16 and their updated values, underline that Eqs. (51)–(53) are indeed fulfilled, see Fig. 22. This provides the exemplary proof, that the results obtained from the evaluation of three-minute creep tests are very robust with respect to different choices of the reference time.

### 4.7. Stress-specific creep strain rate at the end of the three-minute load plateau

The stress-specific creep strain rate at the end of the three-minute load plateau is introduced as a quantity which is independent of the stress imposed during creep testing, and indirectly proportional to $E_c\,[\tau_{ref}]^{\beta}$, which renders it invariant with respect to changes of the reference time, see Eq. (53) and Fig. 22(b). It is equal to the slope of the creep strain history right before unloading, i.e. at $\tau = \tau_3^-$, see Fig. 23, divided by the stress increment applied during the three-minute creep test:

$$\dot{J}_{3\,\mathrm{min}} = \frac{\dot{\varepsilon}(\tau_3^-)}{\sigma(\tau_2) - \sigma(\tau_1)}\,, \tag{54}$$

note that $\tau_1$ and $\tau_2$ denote the time instants at the beginning and at the end of the loading process. In order to express $\dot{\varepsilon}(\tau_3^-)$ in Eq. (54) as a function of $E_c$, $\beta$, and $\tau_{ref}$, Eq. (25) is derived with respect to $\tau$, and the obtained expression is evaluated for $\tau = \tau_3^-$. Inserting the result into Eq. (54) and accounting for $\dot{\sigma}_2 = -\dot{\sigma}_1$ as well as for $\dot{\sigma}_1\,[\tau_2 - \tau_1] = \sigma(\tau_2) - \sigma(\tau_1)$ yields the stress-specific creep strain rate at the end of the three-minute load plateau as

$$\dot{J}_{3\,\mathrm{min}} = \frac{1}{E_c\,[\tau_2 - \tau_1]}\left\{\left[\frac{\tau_3^- - \tau_1}{\tau_{ref}}\right]^{\beta} - \left[\frac{\tau_3^- - \tau_2}{\tau_{ref}}\right]^{\beta}\right\}\,. \tag{55}$$

$\dot{J}_{3\,\mathrm{min}}$ according to Eq. (55) is evaluated for all of the performed three-minute creep tests, using the creep moduli and the creep exponents documented in Section 3.6, see Fig. 24. The values of $\dot{J}_{3\,\mathrm{min}}$

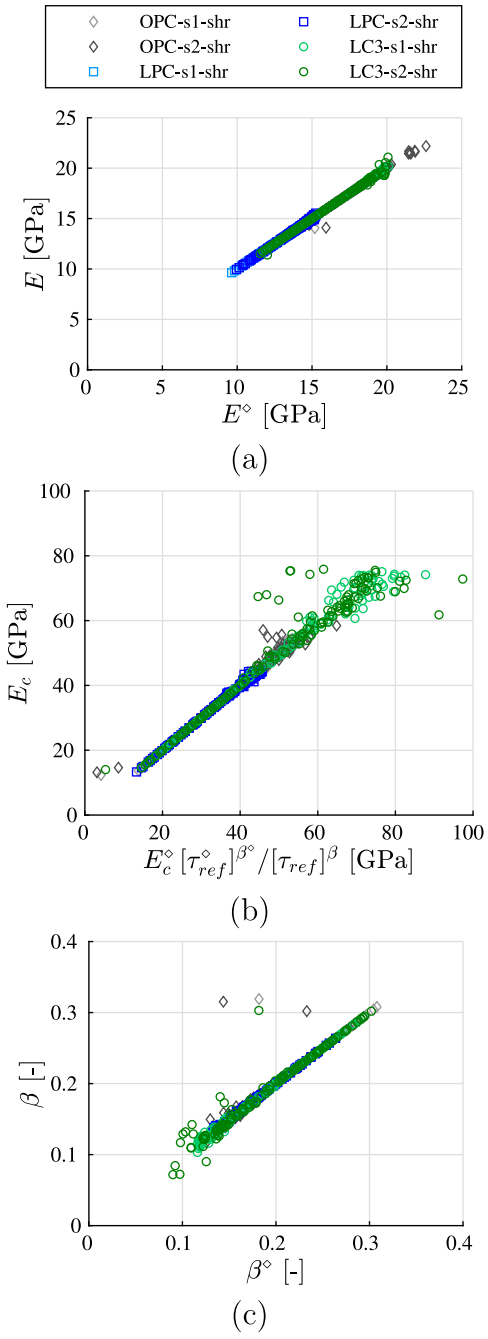


**Fig. 22.** Correlation of identified values of (a) the elastic modulus, (b) the creep modulus, and (c) the creep exponent, when comparing results obtained with $\tau_{ref}$ = 86,400 s and with $\tau^{\diamond}_{ref}$ = 180 s, respectively.

decrease monotonically with increasing material age. The largest values are those of the LPC paste throughout the entire testing period. This implies that the LPC paste creeps more than the OPC and LC3 pastes at the same material age. The values of $\dot{J}_{3\,\mathrm{min}}$ of the OPC paste are some 15% smaller than that of the LPC paste. The LC3 paste exhibits larger values of $\dot{J}_{3\,\mathrm{min}}$ than the OPC paste during the first 3.25 days of hydration, and smaller values thereafter. This implies that the LC3 paste creeps less than the OPC paste already during the second half of the first week after production.

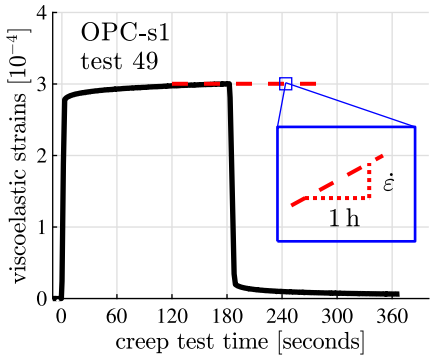


**Fig. 23.** Creep strain rate at the end of the three-minute load plateau.

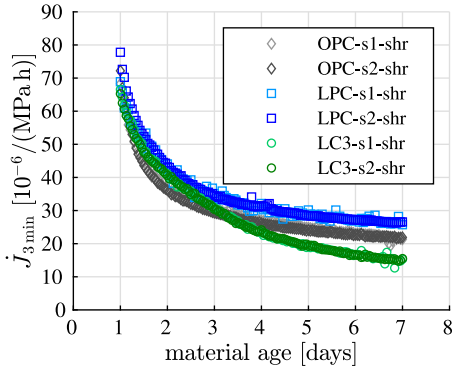


**Fig. 24.** Stress-specific creep strain rate at the end of the three-minute load plateau as a function of material age.

## 5. Discussion of the influence of the pozzolanic reaction on the evolution of shrinkage, elastic stiffness, and creep of the LC3 paste

The early-age evolution of macroscopic mechanical properties of cementitious materials is a result of the hydration-driven evolution of their microstructures. This provides the motivation to discuss the relation between the *macroscopic* shrinkage, elastic stiffness, and creep of the LC3 paste, as determined by means of hourly three-minute creep testing, and their *microstructural* phase assemblage, including both the solid constituents and the pores. As references, OPC and LPC pastes are discussed first.

All here-studied macroscopic properties of the OPC and LPC pastes evolve in a qualitatively similar fashion, because of the chemical similarity of both materials. Quantitative difference can be explained by the larger porosity of the LPC paste, resulting from a larger initial water-to-*cement* mass ratio [52,53]. From 1 to 7 days after paste production, the volume fraction of capillary pores of the OPC paste decreases from 0.32 to 0.23, and that of the LPC paste from 0.37 to 0.29, see Appendix D.

The evolution of the macroscopic properties of the LC3 paste is qualitatively and quantitatively different to those of the OPC and LPC pastes. This is the result of the pozzolanic reaction and the associated reduction of the porosity.

Mercury Intrusion Porosimetry (MIP) was used to analyze pore entry radii and the total porosity of LC3 and OPC pastes [1,15,54,55]. The work of Zunino et al. [55] provides specifically valuable insight into the porosity development during the first week after material production. Therein, it is shown that the total porosity of LC3 pastes is significantly larger than that of an OPC reference paste at a material age of 1 day, and that this difference decreases progressively, such that the total porosity of LC3 pastes is only slightly larger than that of an OPC reference some 7 days after paste production.

Due to the pozzolanic reaction, the hydration products of the LC3 paste are more diverse than those of the OPC and LPC pastes. The reaction consumes Portlandite, Aluminum-Silicate, limestone, and water to produce C-(A-)S-H [56] and AFm phases (= alumina, ferric oxide, monosubstituted phases) [1,57,58]. The AFm phases include (calcium) hemi- or mono-carboaluminates, hydroxy-AFm, and strätlingite [58–60]. In order to gain deeper insight into LC3 hydration, thermodynamic modeling by means of CemGEMS [61] is performed.

### 5.1. Evolution of the phase assemblage of OPC, LPC, and LC3 pastes: thermodynamic modeling using CemGEMS

CemGEMS [61] is a tool for thermodynamic modeling of cementitious materials. It computes chemical speciation by Gibbs energy minimization (GEM) [62]. OPC, LPC, and LC3 recipes according to Tables 1, 2, and 3 are input for CemGEMS computations. Limestone is considered as $CaCO_3$. Calcined clay is defined based on mean values of the weight percentages listed in Table 2. Cement hydration is modeled using the modified Parrot Killoh (mPK) model [63,64]. This provides the microstructural phase assemblage of OPC, LPC, and LC3 pastes as a function of the CemGEMS-simulated material age, see Fig. 25. For the sake of simplicity, several material phases are grouped together: "CEM I" is the group name for Alite, Belite, Aluminate, Ferrite, Periclase, Calcite, Fluorite, and Gypsum. "Other hydrates" is the group name for Hydrogarnet, Apatite, Titanite, Hydrotalcite, Brucite, and Manganite. In addition, "AFm" is the abbreviation for MonocarbonateH11.

The CemGEMS-simulated material age is distinguished from the actual material age, because the simulated reaction kinetics do not necessarily reproduce the experimental ones with very high accuracy. The following discussion of CemGEMS results is focused on relative amounts of Portlandite and AFm phases, which are significantly different in OPC and LPC pastes on the one hand, and the LC3 paste on the other hand.

The Portlandite content of the OPC and LPC pastes increases monotonically with the CemGEMS-simulated material age, see Fig. 26. Both binders exhibit virtually the same amount of Portlandite per 100 g of initial OPC. The LC3 paste develops the smallest amount of Portlandite. It increases until the CemGEMS-simulated material age of 2 days, and decreases thereafter, emphasizing the consumption of Portlandite in the pozzolanic reaction.

The content of AFm phases of all three materials increases monotonically with the CemGEMS-simulated material age, see Fig. 27. The LC3 paste develops the largest amount of AFm phases per 100 g of initial OPC. The OPC and LPC pastes exhibit a significantly smaller amount of AFm phases.

These CemGEMS results underline that the microstructural phase composition of the LC3 paste differs significantly from that of the OPC/LPC pastes. The dissolution of Portlandite, the precipitation of AFm phases, and space filling (= reduction of porosity) due to the production of C-(A-)S-H phases, all resulting from the pozzolanic reaction, manifest themselves macroscopically in the LC3-specific shrinkage, elastic stiffness, and creep evolutions.

### 5.2. Microstructural origins of the macroscopic shrinkage evolution of the LC3 paste

The S-shaped evolution of macroscopic shrinkage of the LC3 paste differs qualitatively from the negatively curved macroscopic shrinkage of the OPC and LPC pastes, see Fig. 15. This difference can be traced back to the dissolution of Portlandite, as explained in the remainder of this subsection.

Chemical shrinkage refers to the fact that reaction products occupy a smaller volume than the reactants [65]. Once a solid skeleton is formed, progressive chemical shrinkage leads to a monotonically increasing negative pressure in the pore water [53]. This is balanced by compressive stresses of the solid skeleton. These pre-stresses are heterogeneously distributed, as explained next.

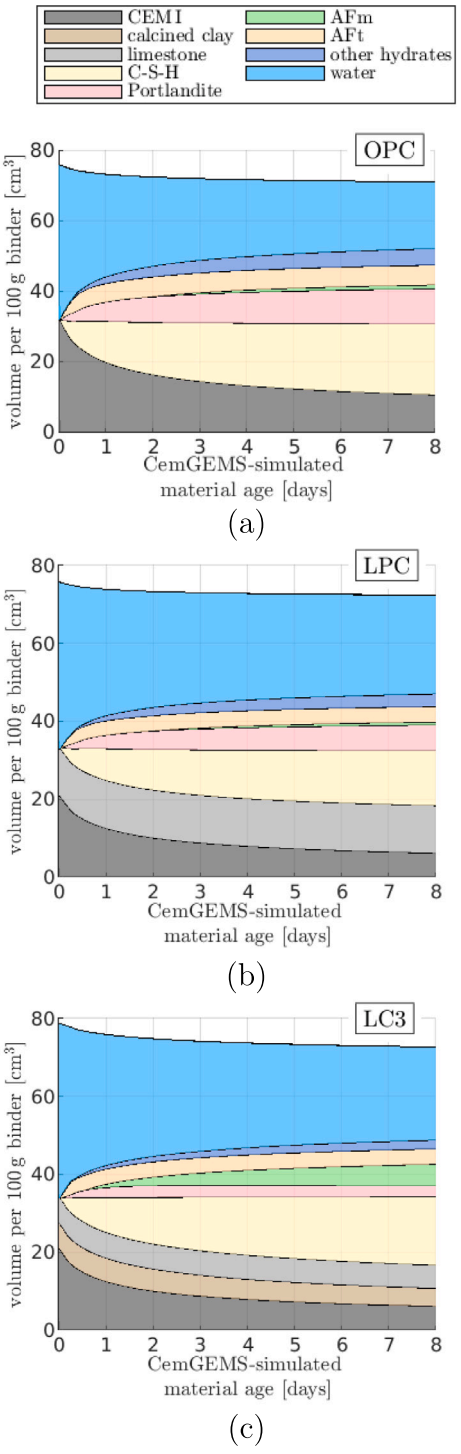


**Fig. 25.** CemGEMS-computed evolution of the volumetric microstructural phase assemblage per 100 g of initial binder: (a) OPC, (b) LPC, and (c) LC3. (For interpretation of the references to color in this figure legend, the reader is referred to the web version of this article.).

Portlandite crystals precipitate free of stresses. Therefore, their pore pressure-related pre-stress is the larger, the earlier they have precipitated, and the larger the negative pressure of the pore water, i.e. the larger the degree of hydration.

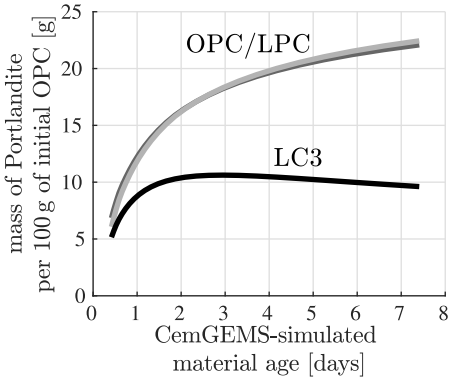


**Fig. 26.** CemGEMS-computed evolution of the mass of Portlandite per 100 g of initial OPC, for the OPC, LPC, and LC3 pastes.

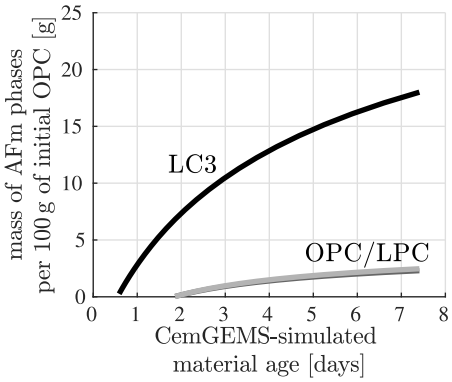


**Fig. 27.** CemGEMS-computed evolution of the mass of the AFm phases per 100 g of initial OPC, for the OPC, LPC, and LC3 pastes.

Portlandite crystals dissolve in the pozzolanic reaction. The associated chemical potential increases with increasing mechanical stress [66], i.e. the likeliness of dissolution of higher-stressed crystals is larger than of lower-stressed crystals [67]. Once a pre-stressed Portlandite crystal dissolves, its pre-stresses are re-distributed. This increases the compressive stress level of the surrounding solid skeleton, which results in increased compressive deformation and, thus, in additional shrinkage.

The precipitation of AFm phases does not counteract this process, because they are formed free of stresses. This line of arguments suggests that the pozzolanic reaction manifests itself macroscopically as a shrinkage-amplifying effect, as illustrated in Fig. 15 and documented in [68] where LC3 mortars were found to exhibit larger shrinkage rates than OPC mortars. Notably, strain increase resulting from Portlandite dissolution was also discussed in [69,70], but from different perspectives and in the context of different material systems.

### *5.3. Microstructural origins of the macroscopic elastic stiffness evolution of the LC3 paste*

The elastic modulus of the LC3 paste is virtually equal to that of the LPC paste one day after production, and it increases thereafter faster than those of the OPC and LPC pastes, such that it is virtually equal to that of the OPC paste seven days after production, see Fig. 18. The loss of elastic stiffness due to the dissolution of Portlandite is virtually balanced by the gain of elastic stiffness due to precipitation of AFm phases, as is explained next.

Both Portlandite and AFm crystals have virtually the same elastic stiffness [71], see Table 8. They have the same platy hexagonal shape, as shown in SEM images, see [55,72–74], respectively. In addition, the micrographs show that both Portlandite and AFm phases precipitate as micron-sized crystals provided that sufficient precipitation space is available. This is the case in very dilute systems or at very early stages of hydration. At later stages, hydration-driven porosity reduction (= space filling) and pore refinement (= pore subdivision) have decreased the available precipitation space, such that smaller crystals are produced. A combined nanoindentation/SEM-EDS study has shown that Portlandite precipitates even in nanoscopic pores [75]. Therefore, Portlandite crystals in OPC pastes exhibit a size distribution spanning over two to three orders of magnitude. A similar but slightly smaller size-distribution is expected for AFm crystals in LC3 pastes, because the pozzolanic reaction starts later than the CEM I reaction, and this implies that the first AFm phases have less space for precipitation compared to the first Portlandite crystals. Still, the volume of dissolved Portlandite appears to be virtually equal to the volume of precipitated AFm phases, compare Figs. 26 and 27 and note the similarity of the mass densities of Portlandite and AFm phases [76,77], see Table 8. Thus, the precipitating AFm phases virtually replace the dissolved Portlandite due to the described volume balance and the equivalence of their elastic stiffness and crystal shape.

**Table 8**
Elastic stiffness, shape, and mass density of Portlandite and AFm crystals.

| | Portlandite | AFm phases |
|---|---|---|
| Elastic modulus | 42.3 GPa [71] | 42.3 GPa [71] |
| Shape | Platy hexagonal [72,73] | Platy hexagonal [55,74] |
| Mass density | 2.23 g/cm$^3$ [76] | 2.17 g/cm$^3$ [77] |

The specific stiffness increase of the LC3 paste from day 1 to day 7 after production is, therefore, rather related to another feature of the pozzolanic reaction, namely the reduction of the porosity due to space filling by C-A-S-H phases [56]. In this context, it is also noteworthy that C-A-S-H phases have virtually the same elastic stiffness as C-S-H [19].

### *5.4. Microstructural origins of the macroscopic creep evolution of the LC3 pastes*

The stress-specific creep strain rate of the LC3 paste is smaller than those of the OPC and LPC pastes, starting some 3.25 days after material production, see Fig. 24. This result can be explained by two effects resulting from the pozzolanic reaction.

Effect 1: The pozzolanic reaction results in additional space filling due to production of C-A-S-H phases. They creep less than C-S-H, as demonstrated in creep tests on concretes made from binary cements containing CEM I and metakaolin [78,79] or calcined clay [79], respectively. Thus, the macroscopic creep compliance of the LC3 paste is reduced relative to the theoretical alternative that the space would have been filled by C-S-H.

Effect 2: The pozzolanic reaction results in the production of AFm phases. In order to explain their creep reducing role, it is recalled that shear sliding of electrically charged C-S-H surfaces, along nanoscopic interfaces filled and lubricated by confined water, is a frequently discussed microstructural mechanism for macroscopic creep of cementitious materials, see e.g. [80–82] and Fig. 28(a). We envision that these interfaces get partly filled by newly formed AFm phases in LC3 materials, see Fig. 28(b), as is explained next. AFm phases exhibit a layered structure [83]. It consists of calcium-aluminate-hydrate plates separated by layers of water and negatively charged ions [59,60]. Also C-S-H exhibit a layered structure [84,85]. It consists of calcium-silicate plates separated by layers of water and positively charged calcium ions, see e.g. [86–88]. Because of these similarities and differences, (i) AFm phases have also been referred to as a “charge-symmetric version of C-S-H” [89], and (ii) it was suggested that AFm phases preferably precipitate on the surface of C-S-H [90,91]. From this chain of arguments, it follows that nanoscopic slit pores between neighboring C-S-H structures are particularly preferred precipitation sites for AFm

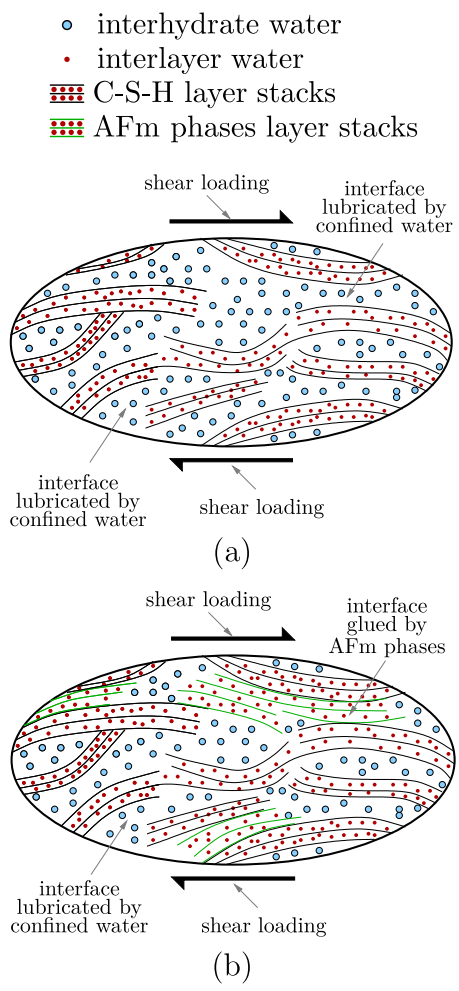


**Fig. 28.** C-S-H-containing part of the nanostructure of the LC3 paste (a) before and (b) after precipitation of AFm phases resulting from the pozzolanic reaction; (a): the nanostructure contains several viscous interfaces between neighboring C-S-H layer stacks, which are lubricated by confined water and develop gliding dislocations upon macroscopic shear loading; (b): some of these interfaces have been filled and, therefore, glued by the precipitation of AFm phase layer stacks, reducing the macroscopic creep compliance; 2D sketch showing a local detail of a 3D isotropic structure.

phases, see Fig. 28. This mode of precipitation of AFm phases fills and, thus, glues formerly viscous interfaces, which contributes to the reduction of the macroscopic creep compliance.

### 5.5. Limitations and future outlook

The present study includes the following limitations. The examined materials were produced from one type of CEM I, one type of limestone, and one type of calcined clay. All pastes were produced with the same initial water-to-binder mass ratio. The clinker replacement ratio in the LPC and LC3 pastes was always equal to $30\%_{mass}$. Mechanical tests were performed from 1 to 7 days after material production. Testing of chemically more diverse materials, production of materials with different initial water-to-binder mass ratios and clinker replacement ratios, the detailed characterization of the microstructural phase assemblage, and multiscale modeling remain topics for future research.

## 6. Conclusions

As regards the here-proposed protocols for hourly three-minute creep testing and evaluation, the following conclusions are drawn:

- Using *six* displacement sensors during hourly three-minute creep testing (rather than *three* sensors as suggested by standard protocols, e.g. [92], or *five* sensors as used e.g. in [20]) results in a redundant setup. Provided that one sensor fails, the affected group of three sensors has to be discarded, but the remaining group of three sensors still provides enough measurements for rigorous test evaluation.
- Numerically efficient *and* reliable quantification of viscoelastic properties, without need to make assumptions, was made possible through an identification procedure organized in two newly proposed steps. Step 1: The creep modulus and the creep exponent are identified such that the modeled strains run as parallel as possible to the experimental strains during the three-minute load plateau. Step 2: The elastic modulus is identified such that the mean difference between modeled and experimental strains vanishes during the three-minute load plateau.
- Shrinkage strains contribute up to 3% to the overall time-dependent strains in the here-performed three-minute creep tests. Explicit consideration of the shrinkage strains during the identification of viscoelastic properties further increases the reliability of the obtained values of the elastic modulus, the creep modulus, and the creep exponent, as underlined by further reduced values of the average strain reproduction errors.
- 20% to 60% of the creep deformation at the end of the 180 s load plateau developed already during the short phase of fast load application. Disregarding creep deformations during loading leads to an underestimation of the elastic modulus by a few percent, and to an overestimation of the creep modulus by a multiplicative factor of up to 2.5.
- The specific value assigned to the reference time of the Power-law-type creep function has no influence on the identification of the elastic modulus and the creep exponent. However, the creep modulus increases with decreasing value assigned to the reference time. Still, the test evaluation approach was shown to be very robust with respect to changes of the reference time: once the viscoelastic properties are identified for one specific choice of the reference time, Eq. (53) allows to compute an updated value of the creep modulus provided that an updated value of the reference time is chosen.

From the interpretation of hourly three-minute creep testing results, the following conclusions are drawn:

- Shrinkage, elastic stiffness, and creep, respectively, of the OPC and LPC pastes evolve qualitatively similar. Quantitative differences can be traced back to the larger porosity of the LPC paste, resulting from a larger initial water-to-cement mass ratio. The qualitatively and quantitatively different behavior of the LC3 paste is governed by the pozzolanic reaction.
- The S-shaped shrinkage evolution of the LC3 paste is explained as follows. The solid skeleton exhibits compressive stresses which balance the negative pressure in the pore water, which results from chemical shrinkage. In the pozzolanic reaction, highly compressed Portlandite crystals dissolve first, because the chemical potential increases with increasing stress. The compressive stresses, which were formerly carried by the dissolved Portlandite crystals, are re-distributed to the surrounding solid skeleton, and this increased compression of the remaining solid microstructure leads to additional macroscopic shrinkage, because new hydration products cannot counteract, as they precipitate free of stresses.
- The elastic stiffness of the LC3 paste increases relatively fast compared to the OPC and LPC pastes in the here-investigated age interval from 1 to 7 days after production. This is primarily a consequence of the reduction of the porosity due to space filling by C-A-S-H phases. The loss of elastic stiffness due to the dissolution of Portlandite, in turn, is virtually balanced by the gain of elastic stiffness due to precipitation of AFm phases.

- The LC3 paste creeps less than the OPC paste, already some three-and-a-half days after material production. This is a result of (i) space filling due to precipitation of C-A-S-H phases which creep less than C-S-H, and (ii) the precipitation of AFm phases in nanoscopic slit pores between neighboring C-S-H structures, which glues formerly viscous interfaces.
- The reduced creep compliance of LC3 materials renders them very attractive for engineering applications in which concrete structures are loaded already at early ages, e.g. prestressed concrete structures.

## CRediT authorship contribution statement

**Sophie J. Schmid:** Writing – review & editing, Writing – original draft, Visualization, Software, Methodology, Investigation, Formal analysis. **Luis Zelaya-Lainez:** Writing – review & editing, Investigation, Formal analysis. **Olaf Lahayne:** Writing – review & editing, Investigation, Formal analysis. **Martin Peyerl:** Writing – review & editing, Formal analysis. **Bernhard Pichler:** Writing – review & editing, Visualization, Supervision, Software, Methodology, Formal analysis, Conceptualization.

## Declaration of competing interest

The authors declare that they have no known competing financial interests or personal relationships that could have appeared to influence the work reported in this paper.

## Acknowledgments

The authors would like to thank Dr. Denis Bézard (Newchem GmbH) for providing the Metaver K calcined clay, Wolfgang Dörner (TU Wien) for support regarding the production of samples, Dr. Johannes Kirnbauer (TU Wien) for help concerning the particle size measurements, and Dr. Markus Königsberger (TU Wien) for interesting discussions. The authors gratefully acknowledge financial support through the MatCH-Maker project which has received funding from the European Union's Horizon Europe research and innovation programme under grant agreement N° 101091687.

## Appendix A. Quantification of $\dot{\sigma}_1$, $\dot{\sigma}_3$, and $\tau_1$, $\tau_2$, $\tau_3$, and $\tau_4$ used in Eq. (24)

Actual values of $\dot{\sigma}_1$ and $\dot{\sigma}_3$ deviate slightly from the nominal values amounting to 2 MPa/s and −1 MPa/s. Actual values are quantified as the slopes of best linear regression functions approximating the central 70% of the stress histories during load application (*la*) and during unloading (*ul*), respectively.

$$\sigma(t) = k_{la}\,\tau + d_{la}\,, \tag{A.1}$$

$$\sigma(t) = k_{ul}\,\tau + d_{ul}\,. \tag{A.2}$$

i.e. $\dot{\sigma}_1 = k_{la}$ and $\dot{\sigma}_3 = k_{ul}$.

$\tau_1$ is the time instant at which Eq. (A.1) is equal to the stress imposed on the specimen prior to the test, $\sigma_{perm}$:

$$\tau_1 = \frac{\sigma_{perm} - d_{la}}{k_{la}}\,, \tag{A.3}$$

where $\sigma_{perm}$ is the average of $\sigma(t_k, \tau)$ according to Eq. (19) within the first nine seconds of the time interval of data acquisition, noting that sensor readings are available also during 10 s prior to loading.

$\tau_2$ is the time instant at which Eq. (A.1) is equal to the stress imposed on the specimen during the load plateau, $\sigma_{plateau}$:

$$\tau_2 = \frac{\sigma_{plateau} - d_{la}}{k_{la}}\,, \tag{A.4}$$

where $\sigma_{plateau}$ is the average of $\sigma(t_k, \tau)$ according to Eq. (19) within the time interval $[\tau_1 + 10\text{ s}\,,\ \tau_1 + 160\text{ s}]$.

**Table D.9**
Initial limestone-to-binder mass ratio and initial water-to-cement mass ratio of the OPC and LPC pastes, as well as computed values of (i) the cement paste-related volume fraction of limestone and (ii) hydration degrees reached under isothermal curing at 25 °C at material ages of 1 day and 7 days, respectively.

| | OPC | LPC |
|---|---|---|
| $(b-c)/b$ | 0.00 | 0.30 |
| $(w/c)$ | 0.45 | 0.64 |
| $f_{\text{ls}}^{\text{cp}}$ | 0.00 | 0.14 |
| $\xi$(1 d) | 0.56 | 0.61 |
| $\xi$(7 d) | 0.74 | 0.85 |

$\tau_3$ is the time instant at which Eq. (A.2) is equal to $\sigma_{plateau}$:

$$\tau_3 = \frac{\sigma_{plateau} - d_{ul}}{k_{ul}}\,, \tag{A.5}$$

$\tau_4$ is the time instant at which Eq. (A.2) is equal to $\sigma_{perm}$:

$$\tau_4 = \frac{\sigma_{perm} - d_{ul}}{k_{ul}}\,. \tag{A.6}$$

## Appendix B. Quantification of $\tau_I$ and $\tau_{II}$ used in Eqs. (30) and (31)

Actual stress readings fluctuate slightly around $\sigma_{plateau}$ during the load plateau. $\tau_I$ is equal to the time instant at which the stress exceeds $\sigma_{plateau}$ for the first time:

$$\tau_I = \min \tau_j \quad \text{for which} \quad \sigma(t_k, \tau_j) > \sigma_{plateau}\,. \tag{B.1}$$

$\tau_{II}$ is equal to the time instant at which the stress exceeds $\sigma_{plateau}$ for the last time:

$$\tau_{II} = \max \tau_j \quad \text{for which} \quad \sigma(t_k, \tau_j) > \sigma_{plateau}\,. \tag{B.2}$$

Notably, $\tau_I$ according to Eq. (B.1) is slightly larger than $\tau_1$ according to Eq. (A.3); and $\tau_{II}$ according to Eq. (B.2) is slightly smaller than $\tau_2$ according to Eq. (A.4).

## Appendix C. Identification of viscoelastic properties from measured strains

See Fig. C.29.

## Appendix D. Quantification of the porosity of OPC and LPC pastes

The porosity of the OPC and LPC paste, respectively, is quantified by means of Powers' hydration model [93]. For LPC, it is adapted to account for limestone as an inert filler material. The cement paste-related volume fraction of the limestone filler reads [23]:

$$f_{\text{ls}}^{\text{cp}} = \frac{\frac{1}{\rho_{ls}}\,\frac{b-c}{c}}{\frac{1}{\rho_{cem}} + \frac{1}{\rho_{\text{H}_2\text{O}}}\,\frac{w}{c} + \frac{1}{\rho_{ls}}\,\frac{b-c}{c}}\,, \tag{D.1}$$

where $\rho_{ls} = 2.7\ \text{g/cm}^3$, $\rho_{cem} = 3.13\ \text{g/cm}^3$, and $\rho_{\text{H}_2\text{O}} = 1.0\ \text{g/cm}^3$ denote the mass densities of limestone, CEM I, and water, and $b$ and $c$ stand for the mass of the binder and CEM I, respectively. Notably, $(b-c)$ corresponds to the mass of limestone. The pore volume fraction $f_{\text{por}}^{\text{cp}}$ is the sum of the cement paste-related volume fractions of water and air, according to the adapted Powers' hydration model [23,93]:

$$f_{\text{por}}^{\text{cp}}(\xi, w/c) = \frac{63(w/c) - 23.15\xi}{20 + 63(w/c)}\,[1 - f_{\text{ls}}^{\text{cp}}]\,, \tag{D.2}$$

where $(w/c)$ is the initial water-to-*cement* mass ratio and $\xi$ denotes the hydration degree. The latter is quantified by dividing the specific heat release according to Fig. 10 by the latent heat of CEM I amounting to 500 J/g [83,94]. The numerical input values of Eqs. (D.1) and (D.2), except the material densities, are summarized in Table D.9.

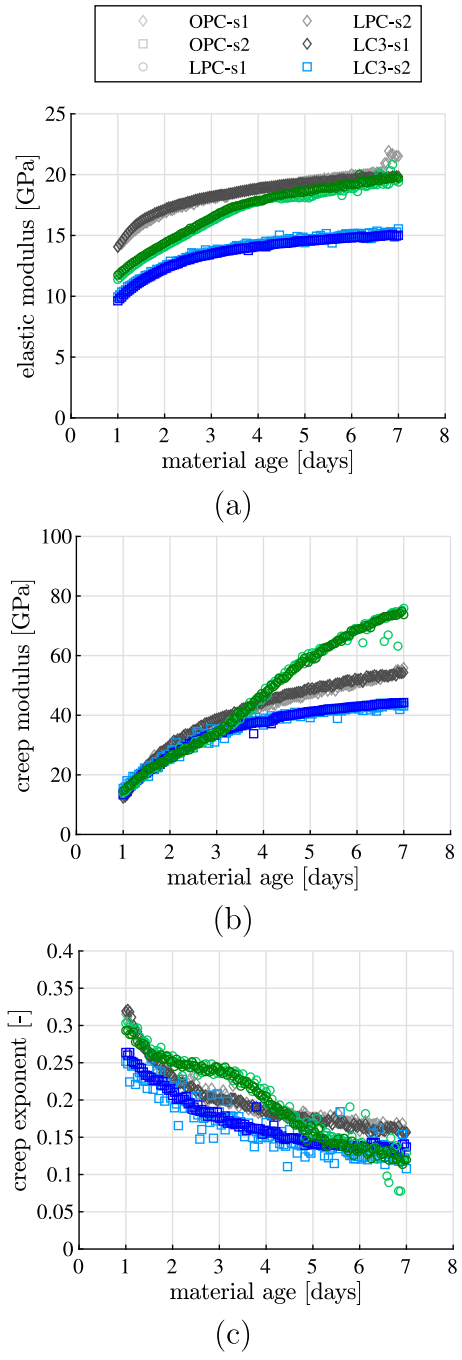


**Fig. C.29.** Hourly performed three-minute creep testing results: identification of viscoelastic properties from measured strains (rather than from viscoelastic strains): (a) elastic modulus $E^\star$, (b) creep modulus $E_c^\star$, (c) creep exponent $\beta^\star$ as functions of the material age.

At a material age of 1 day, the pore volume fraction amounts to $f_{\text{por}}^{\text{OPC}} = 0.32$ for OPC and to $f_{\text{por}}^{\text{LPC}} = 0.37$ for LPC. At a material age of 7 days, the pore volume fraction amounts to $f_{\text{por}}^{\text{OPC}} = 0.23$ for OPC and to $f_{\text{por}}^{\text{LPC}} = 0.29$ for LPC.

## Data availability

Data will be made available on request.

## References

[1] M. Antoni, J. Rossen, F. Martirena, K. Scrivener, Cement substitution by a combination of metakaolin and limestone, Cem. Concr. Res. (ISSN: 0008-8846) 42 (12) (2012) 1579–1589.

[2] K.L. Scrivener, V.M. John, E.M. Gartner, Eco-efficient cements: Potential economically viable solutions for a low-CO2 cement-based materials industry, Cem. Concr. Res. 114 (2018) 2–26.

[3] L. Vizcaíno-Andrés, S. Sánchez-Berriel, S. Damas-Carrera, A. Pérez-Hernández, K. Scrivener, J. Martirena-Hernández, Industrial trial to produce a low clinker, low carbon cement, Mater. Constr. 65 (317) (2015).

[4] J. Sun, F. Zunino, K. Scrivener, Hydration and phase assemblage of limestone calcined clay cements (LC3) with clinker content below 50%, Cem. Concr. Res. 177 (2024) 107417.

[5] K. Scrivener, F. Martirena, S. Bishnoi, S. Maity, Calcined clay limestone cements (LC3), Cem. Concr. Res. 114 (2018) 49–56.

[6] EPFL STI IMX LMC MXG 233, Limestone calcined clay cement, 2024, https://lc3.ch/why-lc3/. (Online Last Access 24 June 2024).

[7] R. Fernandez, F. Martirena, K.L. Scrivener, The origin of the pozzolanic activity of calcined clay minerals: A comparison between kaolinite, illite and montmorillonite, Cem. Concr. Res. (ISSN: 0008-8846) 41 (1) (2011) 113–122.

[8] F. Avet, R. Snellings, A. Alujas Diaz, M. Ben Haha, K. Scrivener, Development of a new rapid, relevant and reliable (R3) test method to evaluate the pozzolanic reactivity of calcined kaolinitic clays, Cem. Concr. Res. (ISSN: 0008-8846) 85 (2016) 1–11.

[9] K. Scrivener, F. Avet, H. Maraghechi, F. Zunino, J. Ston, W. Hanpongpun, A. Favier, Impacting factors and properties of limestone calcined clay cements (LC3), Green Mater. 7 (1) (2018) 3–14.

[10] F. Zunino, K. Scrivener, The influence of the filler effect on the sulfate requirement of blended cements, Cem. Concr. Res. (ISSN: 0008-8846) 126 (2019) 105918.

[11] S. Ferreiro, D. Herfort, J. Damtoft, Effect of raw clay type, fineness, water-to-cement ratio and fly ash addition on workability and strength performance of calcined clay – Limestone Portland cements, Cem. Concr. Res. 101 (2017) 1–12.

[12] T.R. Muzenda, P. Hou, S. Kawashima, T. Sui, X. Cheng, The role of limestone and calcined clay on the rheological properties of LC3, Cem. Concr. Compos. 107 (2020) 103516.

[13] N. Nair, K. Mohammed Haneefa, M. Santhanam, R. Gettu, A study on fresh properties of limestone calcined clay blended cementitious systems, Constr. Build. Mater. 254 (2020).

[14] S. Bishnoi, S. Maity, A. Mallik, S. Joseph, S. Krishnan, Pilot scale manufacture of limestone calcined clay cement: The Indian experience, Indian Concr. J. 88 (6) (2014) 22–28.

[15] Y. Dhandapani, M. Santhanam, Assessment of pore structure evolution in the limestone calcined clay cementitious system and its implications for performance, Cem. Concr. Compos. 84 (2017) 36–47.

[16] A.C. Emmanuel, P. Haldar, S. Maity, S. Bishnoi, Second pilot production of limestone calcined clay cement in India: The experience, Indian Concr. J. 90 (5) (2016) 57–63.

[17] Y. Dhandapani, T. Sakthivel, M. Santhanam, R. Gettu, R.G. Pillai, Mechanical properties and durability performance of concretes with Limestone Calcined Clay Cement (LC3), Cem. Concr. Res. 107 (2018) 136–151.

[18] R. Rocha Ribeiro, M.I.C. Sousa, J.H.d.S. Rêgo, R.d. Lameiras, Innovative low-cost system for early age E-modulus monitoring of cement pastes: Validation and application to nanosilica-added and limestone-calcined clay cements, Mater. Struct. 55 (1) (2022) 1–16.

[19] J. Ston, K. Scrivener, Basic creep of limestone–calcined clay cements: An experimental and numerical approach, Theor. Appl. Fract. Mech. 103 (2019) 102270.

[20] M. Irfan-ul Hassan, B. Pichler, R. Reihsner, C. Hellmich, Elastic and creep properties of young cement paste, as determined from hourly repeated minute-long quasi-static tests, Cem. Concr. Res. 82 (2016) 36–49.

[21] B. Delsaute, C. Boulay, S. Staquet, Creep testing of concrete since setting time by means of permanent and repeated minute-long loadings, Cem. Concr. Compos. 73 (2016) 75–88.

[22] M. Königsberger, M. Irfan-ul Hassan, B. Pichler, C. Hellmich, Downscaling based identification of nonaging power-law creep of cement hydrates, J. Eng. Mech. 142 (12) (2016) 04016106.

[23] L. Göbel, A. Osburg, B. Pichler, The mechanical performance of polymer-modified cement pastes at early ages: Ultra-short non-aging compression tests and multiscale homogenization, Constr. Build. Mater. 173 (2018) 495–507.

[24] A. Naqi, B. Delsaute, M. Königsberger, S. Staquet, Monitoring early age elastic and viscoelastic properties of alkali-activated slag mortar by means of repeated minute-long loadings, Dev. Built Environ. 16 (2023) 100275.

[25] M. Irfan-ul Hassan, M. Königsberger, R. Reihsner, C. Hellmich, B. Pichler, How water-aggregate interactions affect concrete creep: Multiscale analysis, J. Nanomech. Micromech. 7 (4) (2017) 04017019.

[26] M. Ausweger, E. Binder, O. Lahayne, R. Reihsner, G. Maier, M. Peyerl, B. Pichler, Early-age evolution of strength, stiffness, and non-aging creep of concretes: Experimental characterization and correlation analysis, Materials 12 (2) (2019) 207.

[27] Y. Gan, M. Vandamme, H. Zhang, Y. Chen, E. Schlangen, K. van Breugel, B. Šavija, Micro-cantilever testing on the short-term creep behaviour of cement paste at micro-scale, Cem. Concr. Res. 134 (2020) 106105.

[28] Y. Gan, M. Vandamme, Y. Chen, E. Schlangen, K. van Breugel, B. Šavija, Experimental investigation of the short-term creep recovery of hardened cement paste at micrometre length scale, Cem. Concr. Res. 149 (2021) 106562.

[29] E. Binder, M. Königsberger, R.D. Flores, H.A. Mang, C. Hellmich, B.L. Pichler, Thermally activated viscoelasticity of cement paste: Minute-long creep tests and micromechanical link to molecular properties, Cem. Concr. Res. 163 (2023) 107014.

[30] N. GmbH, 2022. https://www.newchem.info/Austria. (Online Last Access 20 May 2022).

[31] I. Fischer, B. Pichler, E. Lach, C. Terner, E. Barraud, F. Britz, Compressive strength of cement paste as a function of loading rate: Experiments and engineering mechanics analysis, Cem. Concr. Res. 58 (2014) 186–200.

[32] P. Karte, M. Hlobil, R. Reihsner, W. Dörner, O. Lahayne, J. Eberhardsteiner, B. Pichler, Unloading-based stiffness characterisation of cement pastes during the second, third and fourth day after production, Strain 51 (2) (2015) 156–169.

[33] C. Kohlhauser, C. Hellmich, Ultrasonic contact pulse transmission for elastic wave velocity and stiffness determination: Influence of specimen geometry and porosity, Eng. Struct. 47 (2013) 115–133.

[34] F. Fedorov, Theory of elastic waves in crystals, Springer Book Arch.-Phys. Astron. (1968).

[35] J.M. Carcione, Wave Fields in Real Media: Wave Propagation in Anisotropic, Anelastic, Porous and Electromagnetic Media, second ed., Elsevier, 2007.

[36] C. Kohlhauser, C. Hellmich, Determination of Poisson's ratios in isotropic, transversely isotropic, and orthotropic materials by means of combined ultrasonic-mechanical testing of normal stiffnesses: Application to metals and wood, Eur. J. Mech. A Solids 33 (2012) 82–98.

[37] P. Lura, O.M. Jensen, K. Van Breugel, Autogenous shrinkage in high-performance cement paste: An evaluation of basic mechanisms, Cem. Concr. Res. 33 (2) (2003) 223–232.

[38] A. Aili, M. Vandamme, J.-M. Torrenti, B. Masson, Is long-term autogenous shrinkage a creep phenomenon induced by capillary effects due to self-desiccation? Cem. Concr. Res. 108 (2018) 186–200.

[39] M.E. Gurtin, E. Sternberg, et al., On the linear theory of viscoelasticity, Arch. Ration. Mech. Anal. 11 (1) (1962) 291–356.

[40] L. Boltzmann, Zur Theorie der elastischen Nachwirkung [On the theory of the elastic aftereffect], Ann. Phys., Lpz. 241 (11) (1878) 430–432.

[41] H. Markovitz, Boltzmann and the beginnings of linear viscoelasticity, Trans. Soc. Rheol. 21 (3) (1977) 381–398.

[42] R. Christensen, Theory of Viscoelasticity, Academic Press, 1982.

[43] I. van Breugel, Relaxation of Young Concrete, Tech. Rep., Delft University of Technology, 1980.

[44] B.T. Tamtsia, J.J. Beaudoin, Basic creep of hardened cement paste: A re-examination of the role of water, Cem. Concr. Res. 30 (9) (2000) 1465–1475.

[45] A. Razgordanisharahi, M. Sorgner, T. Pilgerstorfer, B. Moritz, C. Hellmich, B.L. Pichler, Realistic long-term stress levels in a deep segmented tunnel lining, from hereditary mechanics-informed evaluation of strain measurements, Tunn. Undergr. Space Technol. 145 (2024) 105602.

[46] F. Deschner, F. Winnefeld, B. Lothenbach, S. Seufert, P. Schwesig, S. Dittrich, F. Goetz-Neunhoeffer, J. Neubauer, Hydration of portland cement with high replacement by siliceous fly ash, Cem. Concr. Res. 42 (10) (2012) 1389–1400.

[47] W.A. Gutteridge, J.A. Dalziel, Filler cement: The effect of the secondary component on the hydration of portland cement: Part 1. A fine non-hydraulic filler, Cem. Concr. Res. 20 (5) (1990) 778–782.

[48] W.A. Gutteridge, J.A. Dalziel, Filler cement: The effect of the secondary component on the hydration of portland cement: Part 2: Fine hydraulic binders, Cem. Concr. Res. 20 (6) (1990) 853–861.

[49] B. Lothenbach, K. Scrivener, R. Hooton, Supplementary cementitious materials, Cem. Concr. Res. (ISSN: 0008-8846) 41 (12) (2011) 1244–1256, Conferences Special: Cement Hydration Kinetics and Modeling, Quebec City, 2009 & CONMOD10, Lausanne, 2010.

[50] M. Frías, M. Sanchez De Rojas, J. Cabrera, The effect that the pozzolanic reaction of metakaolin has on the heat evolution in metakaolin-cement mortars, Cem. Concr. Res. 30 (2) (2000) 209–216.

[51] M.S. Meddah, M.C. Lmbachiya, R.K. Dhir, Potential use of binary and composite limestone cements in concrete production, Constr. Build. Mater. 58 (2014) 193–205.

[52] M. Zhang, C. Tam, M. Leow, Effect of water-to-cementitious materials ratio and silica fume on the autogenous shrinkage of concrete, Cem. Concr. Res. 33 (10) (2003) 1687–1694.

[53] P. Acker, Swelling, shrinkage and creep: a mechanical approach to cement hydration, Mater. Struct. 37 (2004) 237–243.

[54] F. Avet, K. Scrivener, Investigation of the calcined kaolinite content on the hydration of Limestone Calcined Clay Cement ($LC^3$), Cem. Concr. Res. (ISSN: 0008-8846) 107 (2018) 124–135.

[55] F. Zunino, K. Scrivener, The reaction between metakaolin and limestone and its effect in porosity refinement and mechanical properties, Cem. Concr. Res. (ISSN: 0008-8846) 140 (2021) 106307.

[56] J. Ambroise, M. Murat, J. Pera, Hydration reaction and hardening of calcined clays and related minerals. IV. Experimental conditions for strength improvement on metakaolinite minicylinders, Cem. Concr. Res. (ISSN: 0008-8846) 15 (1) (1985) 83–88.

[57] V. Bonavetti, V. Rahhal, E. Irassar, Studies on the carboaluminate formation in limestone filler-blended cements, Cem. Concr. Res. 31 (6) (2001) 853–859.

[58] K. De Weerdt, M.B. Haha, G. Le Saout, K.O. Kjellsen, H. Justnes, B. Lothenbach, Hydration mechanisms of ternary portland cements containing limestone powder and fly ash, Cem. Concr. Res. 41 (3) (2011) 279–291.

[59] T. Matschei, B. Lothenbach, F. Glasser, The AFm phase in Portland cement, Cem. Concr. Res. 37 (2) (2007) 118–130.

[60] L.G. Baquerizo, T. Matschei, K.L. Scrivener, M. Saeidpour, L. Wadsö, Hydration states of AFm cement phases, Cem. Concr. Res. 73 (2015) 143–157.

[61] D.A. Kulik, F. Winnefeld, A. Kulik, G.D. Miron, B. Lothenbach, CemGEMS – an easy-to-use web application for thermodynamic modelling of cementitious materials, RILEM Tech. Lett. 6 (2021) 36–52.

[62] CemGEMS development team, 2024. https://cemgems.org/. (Online Last Access 14 March 2024).

[63] L. Parrot, D. Killoh, Prediction of cement hydration, in: Proceedings of the British Ceramic Society, Vol. 35, 1984, pp. 41–53.

[64] B. Lothenbach, G. Le Saout, E. Gallucci, K. Scrivener, Influence of limestone on the hydration of Portland cements, Cem. Concr. Res. (ISSN: 0008-8846) 38 (6) (2008) 848–860.

[65] H. Le Chatelier, Sur les changements de volume qui accompagnent le durcissement des ciments, Bull. Soc. l'encourag. Pour l'Ind. Natl. 5 (1900).

[66] D.J. Srolovitz, On the stability of surfaces of stressed solids, Acta Metall. 37 (2) (1989) 621–625.

[67] D. Koehn, D.K. Dysthe, B. Jamtveit, Transient dissolution patterns on stressed crystal surfaces, Geochim. Cosmochim. Acta 68 (16) (2004) 3317–3325.

[68] G. Medjigbodo, E. Rozière, K. Charrier, L. Izoret, A. Loukili, Hydration, shrinkage, and durability of ternary binders containing Portland cement, limestone filler and metakaolin, Constr. Build. Mater. 183 (2018) 114–126.

[69] T.C. Powers, A hypothesis on carbonation shrinkage, J. PCA Res. Dev. Lab. 4 (2) (1962) 40–50.

[70] M. Jensen, P.F. Hansen, Autogenous deformation and change of the relative humidity in silica fume-modified cement paste, Mater. J. 93 (6) (1996) 539–543.

[71] C.-J. Haecker, E.J. Garboczi, J.W. Bullard, R. Bohn, Z. Sun, S.P. Shah, T. Voigt, Modeling the linear elastic properties of Portland cement paste, Cem. Concr. Res. 35 (10) (2005) 1948–1960.

[72] C. Rodriguez-Navarro, E. Hansen, W.S. Ginell, Calcium hydroxide crystal evolution upon aging of lime putty, J. Am. Ceram. Soc. 81 (11) (1998) 3032–3034.

[73] W. Franus, R. Panek, M. Wdowin, SEM investigation of microstructures in hydration products of Portland cement, in: 2nd International Multidisciplinary Microscopy and Microanalysis Congress: Proceedings of InterM, October 16-19, 2014, Springer, 2015, pp. 105–112.

[74] R. Hay, K. Celik, Performance enhancement and characterization of limestone calcined clay cement (LC3) produced with low-reactivity kaolinitic clay, Constr. Build. Mater. 392 (2023) 131831.

[75] J.J. Chen, L. Sorelli, M. Vandamme, F.-J. Ulm, G. Chanvillard, A Coupled nanoindentation/SEM-EDS study on low water/cement ratio portland cement paste: evidence for C–S–H/$Ca(OH)_2$ nanocomposites, J. Am. Ceram. Soc. 93 (5) (2010) 1484–1493.

[76] Geolitho Stiftung gemeinnützige GmbH, Portlandite, 2024, https://www.mineralienatlas.de/lexikon/index.php/MineralData?mineral=Portlandite. (online; accessed 20 September 2024).

[77] D. Kulik, G. Miron, B. Lothenbach, F. Winnefeld, M. Zajac, B. Huet, F. Georget, CemGEMS web app, 2018, https://cemgems.org/. (Online Accessed 27 January 2022).

[78] J. Brooks, M.M. Johari, Effect of metakaolin on creep and shrinkage of concrete, Cem. Concr. Compos. 23 (6) (2001) 495–502.

[79] S.B. dos Santos, L.C.P. da Silva Filho, J.L. Calmon, Early-age creep of mass concrete: Effects of chemical and mineral admixtures, ACI Mater. J. 109 (5) (2012) 1.

[80] ACI Committee 209 – Creep and Shrinkage, Report on Factors Affecting Shrinkage and Creep of Hardened Concrete, Tech. Rep., American Concrete Institute, 2005.
[81] M. Shahidi, B. Pichler, C. Hellmich, Viscous interfaces as source for material creep: A continuum micromechanics approach, Eur. J. Mech. A Solids 45 (2014) 41–58.
[82] M. Haist, T. Divoux, K.J. Krakowiak, J. Skibsted, R.J.-M. Pellenq, H.S. Müller, F.-J. Ulm, Creep in reactive colloidal gels: A nanomechanical study of cement hydrates, Phys. Rev. Res. 3 (4) (2021) 043127.
[83] H.F. Taylor, et al., Cement Chemistry, second ed., Thomas Telford London, 1997.
[84] R.F. Feldman, P.J. Sereda, A model for hydrated portland cement paste as deduced from sorption-length change and mechanical properties, Matér. Constr. 1 (1968) 509–520.
[85] H.M. Jennings, A model for the microstructure of calcium silicate hydrate in cement paste, Cem. Concr. Res. 30 (1) (2000) 101–116.
[86] C. Labbez, B. Jönsson, I. Pochard, A. Nonat, B. Cabane, Surface charge density and electrokinetic potential of highly charged minerals: experiments and Monte Carlo simulations on calcium silicate hydrate, J. Phys. Chem. B 110 (18) (2006) 9219–9230.
[87] R.J.-M. Pellenq, A. Kushima, R. Shahsavari, K.J. Van Vliet, M.J. Buehler, S. Yip, F.-J. Ulm, A realistic molecular model of cement hydrates, Proc. Natl. Acad. Sci. 106 (38) (2009) 16102–16107.
[88] C. Labbez, I. Pochard, B. Jönsson, A. Nonat, CSH/solution interface: Experimental and Monte Carlo studies, Cem. Concr. Res. 41 (2) (2011) 161–168.
[89] A. Gmira, M. Zabat, R.M. Pellenq, H. Van Damme, Microscopic physical basis of the poromechanical behavior of cement-based materials, Mater. Struct. 37 (2004) 3–14.
[90] M.D. Andersen, H.J. Jakobsen, J. Skibsted, A new aluminium-hydrate species in hydrated portland cements characterized by 27Al and 29Si MAS NMR spectroscopy, Cem. Concr. Res. 36 (1) (2006) 3–17.
[91] E. L'Hôpital, B. Lothenbach, G. Le Saout, D. Kulik, K. Scrivener, Incorporation of aluminium in calcium-silicate-hydrates, Cem. Concr. Res. 75 (2015) 91–103.
[92] ASTM International Committee C09 on Concrete and Concrete Aggregates, ASTM C469/C469M-14 Standard Test Method for Static Modulus of Elasticity and Poisson's Ratio of Concrete in Compression, ASTM International, 2014.
[93] T.C. Powers, T.L. Brownyard, Studies of the physical properties of hardened Portland cement paste, in: Journal Proceedings, Vol. 43, 1946, pp. 101–132.
[94] J. Byfors, Plain Concrete at Early Ages, Swedish Cement and Concrete Research Institute, Stockholm, Sweden, 1980.